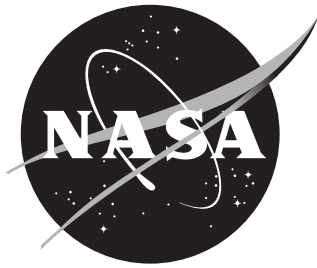


NASA/TP-2014-218399



Physics Based Model for Cryogenic Chardown and Loading. Part IV: Code Structure

D. G. Luchinsky
Ames Research Center, Moffett Field, California

V. N. Smelyanskiy
Ames Research Center, Moffett Field, California

B. Brown
Kennedy Space Center, Florida

NASA STI Program . . . in Profile

Since its founding, NASA has been dedicated to the advancement of aeronautics and space science. The NASA scientific and technical information (STI) program plays a key part in helping NASA maintain this important role.

The NASA STI Program operates under the auspices of the Agency Chief Information Officer. It collects, organizes, provides for archiving, and disseminates NASA's STI. The NASA STI Program provides access to the NASA Aeronautics and Space Database and its public interface, the NASA Technical Report Server, thus providing one of the largest collection of aeronautical and space science STI in the world. Results are published in both non-NASA channels and by NASA in the NASA STI Report Series, which includes the following report types:

- **TECHNICAL PUBLICATION.**
Reports of completed research or a major significant phase of research that present the results of NASA programs and include extensive data or theoretical analysis. Includes compilations of significant scientific and technical data and information deemed to be of continuing reference value. NASA counterpart of peer-reviewed formal professional papers, but having less stringent limitations on manuscript length and extent of graphic presentations.
- **TECHNICAL MEMORANDUM.**
Scientific and technical findings that are preliminary or of specialized interest, e.g., quick release reports, working papers, and bibliographies that contain minimal annotation. Does not contain extensive analysis.
- **CONTRACTOR REPORT.**
Scientific and technical findings by NASA-sponsored contractors and grantees.

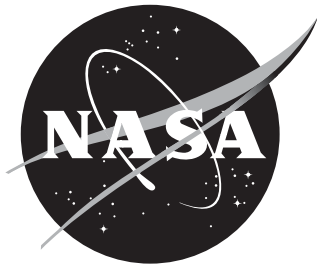
- **CONFERENCE PUBLICATION.**
Collected papers from scientific and technical conferences, symposia, seminars, or other meetings sponsored or co-sponsored by NASA.
- **SPECIAL PUBLICATION.**
Scientific, technical, or historical information from NASA programs, projects, and missions, often concerned with subjects having substantial public interest.
- **TECHNICAL TRANSLATION.**
English- language translations of foreign scientific and technical material pertinent to NASA's mission.

Specialized services also include creating custom thesauri, building customized databases, and organizing and publishing research results.

For more information about the NASA STI Program, see the following:

- Access the NASA STI program home page at <http://www.sti.nasa.gov>
- E-mail your question via the Internet to help@sti.nasa.gov
- Fax your question to the NASA STI Help Desk at 443-757-5803
- Phone the NASA STI Help Desk at 443-757-5802
- Write to:
NASA STI Help Desk
NASA Center for Aerospace Information
7115 Standard Drive
Hanover, MD 21076-1320

NASA/TP-2014-218399



Physics Based Model for Cryogenic Chardown and Loading. Part IV: Code Structure

D. G. Luchinsky
Ames Research Center, Moffett Field, California

V. N. Smelyanskiy
Ames Research Center, Moffett Field, California

B. Brown
Kennedy Space Center, Florida

National Aeronautics and
Space Administration

Ames Research Center
Moffett Field, California 94035-2199

November 2014

Acknowledgments

We are grateful to Charlie Goodrich for the extended discussions and useful comments.

The use of trademarks or names of manufacturers in this report is for accurate reporting and does not constitute an official endorsement, either expressed or implied, of such products or manufacturers by the National Aeronautics and Space Administration.

Available from:

NASA Center for AeroSpace Information
7115 Standard Drive
Hanover, MD 21076-1320
443-757-5802

Abstract

This is the fourth report in a series of technical reports that describe separated two-phase flow model application to the cryogenic loading operation. In this report we present the structure of the code. The code consists of five major modules: (i) geometry module; (ii) solver; (iii) material properties; (iv) correlations; and finally (v) stability control module. The two key modules - solver and correlations - are further divided into a number of submodules. Most of the physics and knowledge databases related to the properties of cryogenic two-phase flow are included into the cryogenic correlations module. The functional form of those correlations is not well established and is a subject of extensive research. Multiple parametric forms for various correlations are currently available. Some of them are included into correlations module as will be described in details in a separate technical report. Here we describe the overall structure of the code and focus on the details of the solver and stability control modules.

1 Introduction

The algorithm of the separated two-phase flow (see also [LuchDG-I]) originates from Liles and Reed [Liles-78], which is in turn based on Harlow and Asden [Harlow-68] all-speed “Implicit Continuous-Fluid Eulerian (ICE)” algorithm. In the current work we implemented the nearly-implicit extension of this algorithm following closely the results of [RELAP5-I]. The ICE-based algorithm is usually called “weakly-compressible”, even though the compressibility effects are fully accounted for in numer-

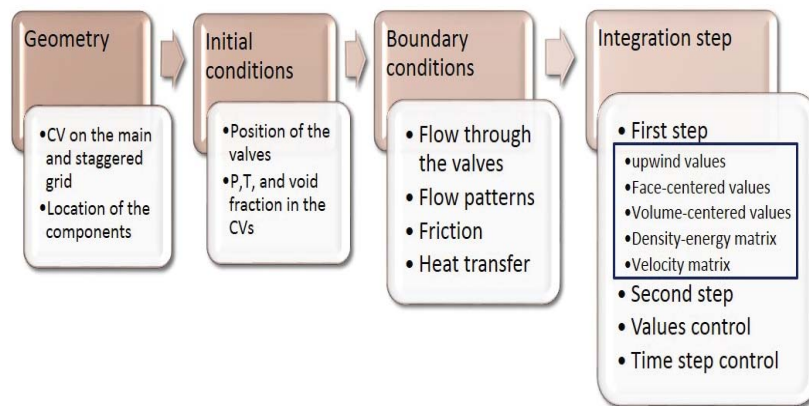


Figure 1. A simplified structure of the code. (top) Four main blocks of the algorithm. Bottom left: Structure of the boundary conditions block. Bottom right: Four main sub-steps of the integration step.

ical discretization. Almost all reactor thermal-hydraulics codes belong to this class and utilize first-order finite-difference donor-cell/upwinding based schemes, implemented on structured staggered meshes, see e.g. [Ransom89, TRACE, Nourgaliev] for further discussion. In what follows we present the details of the algorithm as it was coded. A simplified structure of the code is shown in the Fig. 1. The algorithm consists of the four main blocks

1. geometry,
2. initial conditions,
3. boundary conditions,
4. one integration step.

The geometry and initial condition blocks are set once in the beginning of the code execution. The last two blocks are repeated in the loop N -steps until integration is completed. These two blocks have a complex structure.

The boundary conditions block includes calculation of the interphase geometry, the heat and mass fluxes at the liquid/gas/wall interphases, mass and energy fluxes through the dump valves and through the input/output valves. This block includes the pressure drop and heat transfer correlations for the two-phase flow. These correlations are based on the flow patterns recognition and have very nontrivial structure that will be described in details in a separate technical report. The integration block consists, in turn, of four main sub-steps:

1. first step of integration,
2. second step of integration,
3. control of the values of dynamical variables,
4. time step control.

The first two sub-steps are designed in the spirit of the predictor-corrector architecture of the nearly-implicit method. The last two sub-steps are developed to deal with multiple instabilities inherent to the two-phase flow algorithms and are essential for the smooth code execution, see e.g. [Nourgaliev, Cordier13, LuchDG-I].

Out of four integration sub-steps the first one has the most nontrivial structure and its details are the key to the successful performance of the algorithm as a whole. It involves calculations of the upwind, face-centered, and volume-centered values of the dynamical variables. The overall stability and accuracy of the algorithm in the quasi-equilibrium limit (no heat transfer) is mainly determined by the solution of the two

matrix equations: (i) matrix equation for the expanded form of the conservation laws for the phasic masses and energies and (ii) matrix equation for the phasic velocities (see Fig. 1).

Before we discuss the structure of each block in more details, we remind for convenience the model equations of the nearly-implicit scheme method.

2 Model

2.1 The model equations

We model cryogenic loading and chilldown using Wallis equations [Wallis69] for a one-dimensional separated two-phase flow. The model consists of a set of conservation laws for the mass, momentum, and energy for the gas

$$\begin{aligned}
(A\alpha\rho_g)_{,t} + (A\alpha\rho_g u_g)_{,x} &= A\Gamma_g \\
(A\alpha\rho_g u_g)_{,t} + (A\alpha\rho_g u_g^2)_{,x} + A\alpha p_{,x} &= -A\alpha\rho_g z_{,x} \\
&\quad - \tau_{gw} l_{wg} - \tau_{gi} l_i + A\Gamma_g u_{ig} \\
(A\alpha\rho_g E_g)_{,t} + (A\alpha\rho_g E_g u_g)_{,x} &= A\alpha p_{,t} - (pA\alpha u_g)_{,x} \\
&\quad + \dot{q}_{gw} l_{wg} + \dot{q}_{gi} l_i + A\Gamma_{ig} H_{ig} + A\Gamma_{wg} H_{wg}
\end{aligned} \tag{1}$$

and for the liquid

$$\begin{aligned}
(A\beta\rho_l)_{,t} + (A\beta\rho_l u_l)_{,x} &= -A\Gamma_g \\
(A\beta\rho_l u_l)_{,t} + (A\beta\rho_l u_l^2)_{,x} + A\beta p_{,x} &= -A\beta\rho_l z_{,x} - \\
&\quad \tau_{lw} l_{wl} - \tau_{li} l_i - A\Gamma_g u_{il} \\
(A\beta E_l \rho_l)_{,t} + (A\beta E_l \rho_l u_l)_{,x} &= A\beta p_{,t} - (pA\beta u_l)_{,x} + \\
&\quad \dot{q}_{lw} l_{wl} + \dot{q}_{li} l_i - A\Gamma_{ig} H_{ig} - A\Gamma_{wg} H_{wg}
\end{aligned} \tag{2}$$

coupled to the equation for the wall temperature

$$\rho_w c_w d_w \frac{\partial T_w}{\partial t} = h_{wg} (T_g - T_w) + h_{wl} (T_l - T_w) + h_{amb} (T_{amb} - T_w). \tag{3}$$

Here p , α , T , and ρ are pressure, temperature, and density of the fluid. E is the total specific energy, H_{ig} and H_{wg} is the specific enthalpy of the gas generated at the interface and near the wall respectively. u is the fluid velocity and h is the heat transfer coefficient. Other model notations are explained in the Section Nomenclature.

2.2 Discretization

The equations (1), (2), and (3) are integrated on a one dimensional grid shown in the Fig. 2. The energy and density conservation equations are integrated over N control volumes centered at locations $L = 1, \dots, N$ shaded by yellow. The momentum equations are integrated over $N - 1$ control volumes of the staggered grid centered at locations $j = 1, \dots, N - 1$ shaded by blue. The equations for the wall temperature are integrated over N control volumes shaded by green.

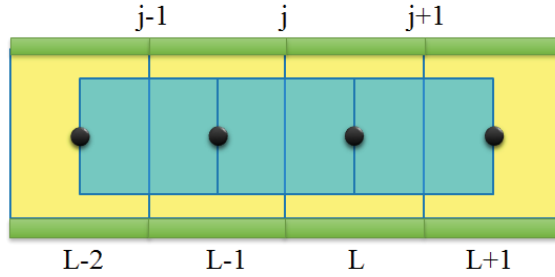


Figure 2. Grid grid with N control volumes shaded by yellow, staggered grid with $N - 1$ control volumes shaded by blue, and N control volumes for the wall shaded by green.

2.3 Brief summary of the nearly implicit scheme

The algorithm described below is a variation of the nearly-implicit method [RELAP5-I] and [RELAP5-VI] (see also [LuchDG-I]).

2.3.1 Boundary conditions

Boundary conditions module includes analysis of the interface geometry, phasic masses, heat fluxes, and flow through the valves. At present this module involves a simplified set of pressure drop and heat transfer correlations based on the effective geometry of conceptually stratified flow (i.e. liquid and gas are assumed to be always stratified). The calculations within this module can be briefly summarized as follows

- determine geometry of the phasic interface;
- calculate frictional losses;
- find heat transfer coefficients at the wall;
- find mass and enthalpy fluxes at the liquid/gas interface;
- calculate mass and enthalpy fluxes through the dump and input/output valves.

The extended version of the boundary conditions module will include pressure drop and heat transfer correlations based on the flow pattern recognition and will be discussed in details in a separate technical report.

2.3.2 First sub-step

The calculations of the velocities, pressure, and provisional values of the masses and energies at the first sub-step of the algorithm is the key to the stable performance of the nearly-implicit method. These calculations

are designed to break limitations of the material CFL and to increase implicitness of the method. This sub-step is structured as a predictor of the fractional time step technique. The CFL limitations are lifted by implicit calculations of the new velocities and pressures in the system. The implicitness is further increased by estimations of the provisional values of the densities, energies, heat and mass transfer coefficients. The calculations can be briefly summarized as follows:

- Calculate upwind, face-centered, and volume-centered velocities;
- Solve expanded equation with respect to pressure in terms of new velocities;
- Substitute this solution into momenta equations and solve resulting block tri-diagonal matrix equation for the new velocities;
- Find new pressure;
- Find provisional values for energies and void fractions using expanded equations;
- Find provisional values of mass fluxes and heat transfer coefficients using provisional values of temperatures obtained.

Corrections to the provisional values of void fractions, densities, and energies are found at the second sub-step of the integration step of the algorithm.

2.3.3 Second sub-step

To find new (corrected) values values of the densities, void fractions, and energies we solve unexpanded conservation equations for the phasic masses and energies using fully implicit method. The solution is reduced to independent solution of four tridiagonal matrices. The values of pressure and velocities in these matrices are taken at the new time step.

2.3.4 Control

Despite the enhanced stability of the nearly-implicit method the instabilities remain a challenging problem. Multiple sources of instabilities in modeling separated two-phase flow include non-hyperbolicity, lack of positivity, and phase appearance/disappearance (see e.g. [LuchDG-I] and references therein). To obtain a reliable and stable execution of the code extended controls of the dynamical variables and of the time step are introduced into the code. These controls include

1. check that void fraction is between 0 and 1;
2. if void fraction is within the predefined range of the boundary values corresponding to the phase appearance/disappearance apply smoothers to the temperatures, densities, and velocities;

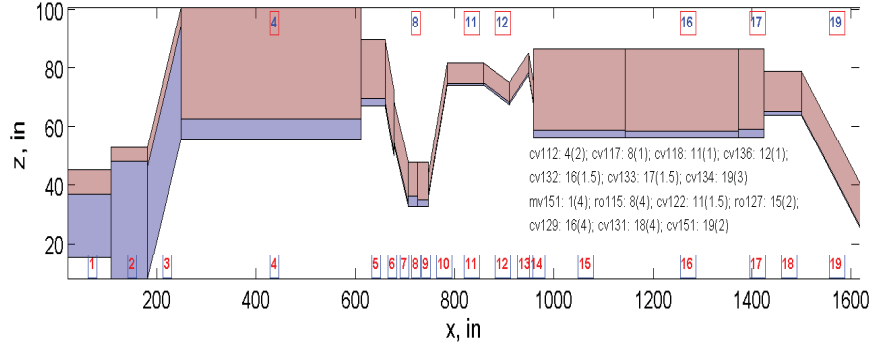


Figure 3. A set of control volumes introduced for the transfer line model of the KSC testbed.

3. check if phasic temperatures are within thermodynamic range;
4. check pressure range;
5. check mass conservation in each control volume;
6. check mass conservation in the system as whole;
7. compare the provisional and final values of phasic densities and energies;
8. if the dynamical variables are outside of the physical range or variation if variables is too large the integration step is repeated with reduced value of the time step $\Delta\tilde{t} = \Delta t/2$, while $\Delta\tilde{t} \geq \Delta t_{min}$.

Once control checks are completed the calculations return to the step 2.3.1. The sub-steps 2.3.1 through 2.3.4 are repeated until final time of the integration $T = \sum_{i=1}^N \Delta\tilde{t}_i$ is reached.

3 Geometry Module

One of the important properties of the method briefly outlined above is the ability to resolve the two-phase flow dynamics and heat transfer for a complex geometry of the pipes. The geometry of the model is defined as an ordered collection of N control volumes $\mathcal{M} = \{CV\}_i^N$. The finite volume mesh \mathcal{M} is characterized by the following constant parameters: (i) length Δx_i , (ii) perimeter l_i , (iii) height h_i , and (iv) inclination angle α_i . The following related geometrical parameters are also frequently used: (v) diameter d_i , (vi) surface area S_i , (vii) volume V_i , and (viii) cross-sectional area A_i .

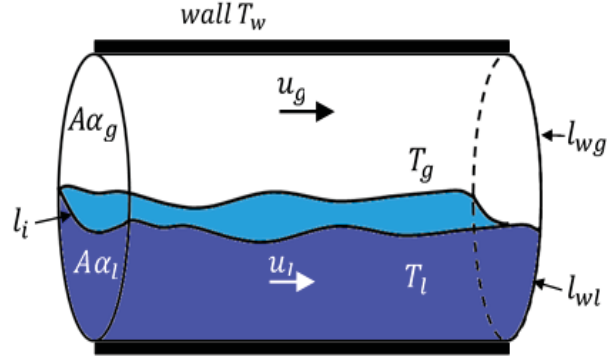


Figure 4. A single control volume of the model.

For example, the control volumes introduced for the cryogenic testbed are shown in the Fig. 3. The volumes are numerated at the bottom of the figure. The blue shaded areas indicate the quantity of liquid in each control volume. A single control volume of the model is shown in the Fig. 4. A number of important geometrical parameters of the control volume that are shown in the figure change every time step and belong to the set of dynamical variables of the system. These parameters are: (i) dry perimeter $l_{gw,i}$, (ii) wetted perimeter $l_{lw,i}$, (iii) interface perimeter $l_{i,i}$, (iv) height of the stratified liquid level $b_{l,i}$.

3.1 Components

In addition to the standard geometrical parameters there is a large number of components that dramatically affect the fluid flow and have to be taken into account in any industrial cryogenic loading system. These components include e.g. valves, bends, filters, fittings, pumps etc. The components are characterized by their location and frictional and heat losses. For example the locations of the valves that control flow in cryogenic testbed at KSC together with location of pressure and temperature sensors are shown in the Fig. 5. The solid black line corresponds to the flow path. The location of the components including dump valves, control valves, and sensors can also be resolved in the figure.

These information is integrated into the code in the form of tables. An example of the table is shown in the Fig. 6.

In this way the information about components can be attributed to each control volume for arbitrary set of control volumes \mathcal{M} . For example the location of the dump valves in the set of control volumes corresponding to the KSC testbed model is shown at the top of the Fig. 3.

The details of the calculations of the source terms that include information about pressure and heat losses in the system components are given the following section.

4 Boundary Conditions Module

Boundary conditions within this report are interpreted in a more general sense than usual. They include not only conditions at the input/output valves, but also conditions at the liquid/gas/wall phasic boundaries and at a liquid/gas interface. Therefore, the current version of the boundary condition module includes calculations of the simplified correlations relations. However, the future versions of the algorithm will have a separate correlation module.

Note, that the boundary conditions for the continuity and energy equations are determined on the grid of the control volumes of the system, while boundary conditions for the momenta equations are defined on the staggered grid. To this end it is convenient to rewrite equations (1), (2) in a matrix form

$$\frac{\partial U}{\partial t} + \frac{\partial F}{\partial x} = S_U, \quad \frac{\partial V}{\partial t} + \frac{\partial G}{\partial x} = S_V. \quad (4)$$

Here the conservative variables are

$$U = \begin{bmatrix} A\alpha\rho_g \\ A\alpha\rho_g E_g \\ A\beta\rho_l \\ A\beta\rho_l E_l \end{bmatrix}, \quad V = \begin{bmatrix} A\alpha\rho_g u_g \\ A\beta\rho_l u_l \end{bmatrix} \quad (5)$$

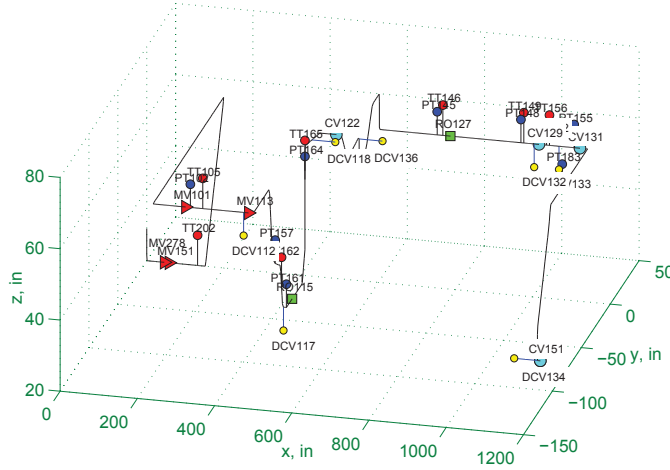


Figure 5. Geometry of the flow path is shown by the solid black line. The dump valves (DCV) are indicated by yellow circles. The control valves (CV) are shown by cyan circles. The temperature sensors (TT) are shown by bike circles and the pressure sensors (PT) are shown by red circles.

		Y	Z	X	D	Comp	K (f*L/D)	Cv
304.2	pipe4_A	0	20	-71.5	4in			
305	To	0	20	-92		MV151	5.95	195
306	To	0	20	-105.5		MV278	2.49	283
308	To	0	20	-149.5		Bend_056	0.192	
309	To	0	29	-149.6		entrance	0.28	
303	pipe3_A	0	20	-53	3in			
310	To	-17.5	20	-81.5		Tee		
311	To	-17.5	20	-100.5		MV150	5.95	130
312	To	-17.5	20	-106.5		MV279	2.84	188
314	To	-17.5	20	-114		Tee		
314.1	To	-17.5	20	-119		Bend_058	0.204	
315	To	-10.5	20	-128.5		Bend_059	0.102	
316	To	-10.5	20	-138.5		Bend_060	0.204	
317	To	-10.5	26	-138.6		entrance	0.28	
Start	pipe6_A	0	20	0	6in			
302	To	0	20	-9		EJ003		
303	To	0	20	-15		TT202		
303	To	0	20	-53		Tee		
304	To	0	20	-56.5		Mass		
304.1	To	0	20	-67.5		Reducer_010	1	
Start	pipe6_B	0	20	0.05	6in			
-0.1	To	0	20	6		Bend	0.09	
0	To	0	25	11		Flange		
1	To	0	58.5	44.5		Flange		
1.1	To	0	68	54		Bend	0.18	
2	To	-12	68	54.05		Flange		
3	To	-33	68	54.1		Support-Oneway		

Figure 6. An example of the table with a list of cryo-testbed components integrated into the model.

and fluxes are

$$F = \begin{bmatrix} A\alpha\rho_g u_g \\ A\alpha u_g (\rho_g E_g + p) \\ A\beta\rho_l u_l \\ A\beta u_l (E_l\rho_l + p) \end{bmatrix}, \quad G = \begin{bmatrix} A\alpha\rho_g u_g^2 \\ A\beta\rho_l u_l^2 \end{bmatrix}. \quad (6)$$

The Boundary Conditions Module is primarily concerned with the calculation of the source terms

$$S_U = \begin{bmatrix} A\Gamma_g - \dot{m}_{vl} \\ A\alpha p_{,t} + \dot{q}_{gw} l_{wg} + \dot{q}_{gi} l_i + A\Gamma_{ig} H_{ig} + A\Gamma_{wg} H_{wg} - \dot{m}_{vl} h_g \\ -A\Gamma_g \\ A\beta p_{,t} + \dot{q}_{lw} l_{wl} + \dot{q}_{li} l_i - A\Gamma_{ig} H_{ig} - A\Gamma_{wg} H_{wg} \end{bmatrix}, \quad (7)$$

$$S_V = \begin{bmatrix} -A\alpha p_{,x} - A\alpha\rho_g z_{,x} - \tau_{gw} l_{wg} - \tau_{gi} l_i + A\Gamma_g u_{ig} \\ +A\beta p_{,x} - A\beta\rho_l z_{,x} - \tau_{lw} l_{wl} - \tau_{li} l_i - A\Gamma_g u_{il} \end{bmatrix}. \quad (8)$$

The source terms (7) are calculated twice during one integration step. Once during the first sub-step and once during the second sub-step. The source terms (8) are calculated only once before the solution of the velocity matrix equation.

The source terms are calculated using a few sub-steps. The first sub-step involves the following calculations:

- determine flow patterns for each control volume;
- calculate geometrical parameters of the flow based on the type of the flow pattern;

- find heat fluxes at the liquid/gas/wall interfaces for the values of thermodynamic variables found at the previous time step;
- determine the mass and enthalpy fluxes using values of the heat fluxes and latent heat of vaporization/condensation;
- find mass/enthalpy fluxes through the dump valves and input/output valves.

Once the terms S_V are calculated, the new values of pressure are found by solving the expanded and modified version of the first equation in (4) with respect to pressure as described in more details in Sec. 5.1.

At the next sub-step the new values of pressure and old values of the thermodynamic variables are used to find source terms in (8). The values of S_V obtained at this sub-step are used to find the new velocities by solving the non-conservative version of the second equation in (4) as discussed in details in Sec. 5.2. The new velocities and new pressures are used to find provisional values of the thermodynamic variables (see Sec. 5.3).

Next, the values of the S_U are updated using provisional temperature and mass fluxes and the conservative form of the first equation in (4) is solved to find new values of thermodynamic variables as described in Sec. 6.

It can be seen from this brief description that all the non-trivial physics of the problem and related calculations are coupled with an analysis of the source terms. Further details of this analysis are discussed in the following few subsections of this section.

4.1 Flow patterns

Mass and heat transfer between the phases of the two-phase flow is closely related to the geometrical patterns formed by the flow. Examples of typical patterns include [Bejan03]

Stratified flow. At low liquid and gas velocities, there is complete separation of the two phases, with the gas in the top and the liquid in the bottom, separated by an undisturbed horizontal interface.

Bubbly flow. In this regime, the gas is dispersed in the form of discrete bubbles in the continuous liquid phase. The shapes and sizes of the bubbles may vary widely, but they are notably smaller than the pipe diameter.

Slug flow. Increasing the gas fraction, bubbles collide and coalesce to form larger bubbles similar in size to the pipe diameter. These have a characteristic hemispherical nose with a blunt tail end, similar to a bullet, and are referred to as Taylor bubbles. Successive bubbles are separated by a liquid slug, which may include smaller entrained

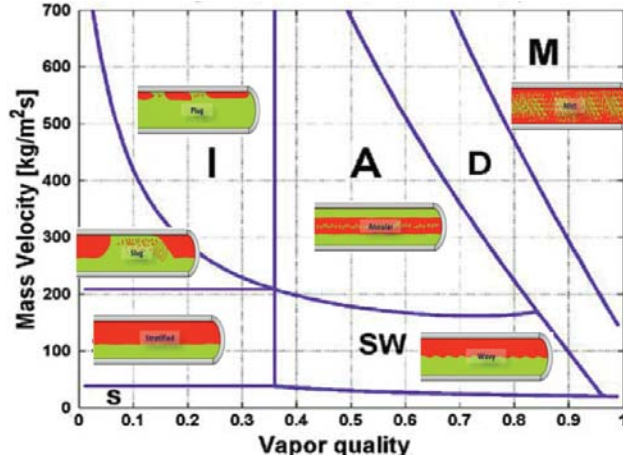


Figure 7. Example of the flow patterns in the two-phase flow. Notations for the flow boundaries are (following [Bejan03]): (A) annular flow; (D) dispersed flow (droplets flowing in the gas); (I) intermittent flow (switches between patterns of slug and annular flow); (M) mist flow; (S) stratified flow; (SW) wavy stratified flow.

bubbles. These bullet-shaped bubbles have a thin film of liquid between them and the channel walls, which may flow downward due to the force of gravity, even though the net flow of liquid is upward.

Annular flow. Here the bulk of the liquid flows as a thin film on the wall with the gas as the continuous phase flowing up the center of the tube, forming a liquid annulus with a gas core whose interface is disturbed by both large-magnitude waves and chaotic ripples. Liquid may be entrained in the high-velocity gas core as small droplets; the liquid fraction entrained may be similar to that in the film. This flow regime is quite stable and is often desirable for system operation and pipe flow.

Mist flow. When the flow rate is increased even further, the annular film becomes very thin, such that the shear of the gas core on the interface is able to entrain all the liquid as droplets in the continuous gas phase (i.e., the inverse of the bubbly flow regime). The wall is intermittently wetted locally by impinging droplets. The droplets in the mist may be too small to be seen without special lighting and/or magnification.

The detailed analysis of the flow patterns goes beyond the scope of the present discussion and will be given in a separate technical report [LuchDG-III]. Here we only provide an example of how flow patterns are determined in practice. Following the results of Kattan et al [Kattan:98a] the boundary for the stratified flow on the plain (\dot{m}, χ)

we have

$$\dot{m}_{strat} = \left\{ \frac{(226.3)^2 A_{lwd} A_{gwd}^2 \rho_G (\rho_L - \rho_G) \mu_L g}{\chi^2 (1 - \chi) \pi^3} \right\}^{1/3} + 20\chi, \quad (9)$$

for the wavy flow one can obtain

$$\dot{m}_{wavy} = \left\{ \frac{16 A_{gwd}^3 g D \rho_L \rho_G}{\chi^2 \pi^2 [1 - (2b_l - 1)^2]^{.5}} \left[\frac{\pi^2}{25 b_l^2} (1 - \chi)^{-F_1(q)} \left(\frac{We}{Fr} \right)_L^{-F_2(q)} + 1 \right] \right\}^{.5} + 50, \quad (10)$$

and for the mist flow the boundary is

$$\dot{m}_{mist} = \left[\frac{7680 A_{gwd}^2 g D \rho_L \rho_G}{\chi^2 \pi^2 \xi_{Ph}} \left(\frac{Fr}{We} \right)_L \right]^{.5}. \quad (11)$$

Here the following parameters were introduced. The friction factor

$$\xi_{Ph} = \left(1.138 + 2 \log \frac{\pi}{1.5 A_{lwd}} \right)^{-2}.$$

The Weber number $We_L = \frac{\dot{m}_l^2 D}{\rho_L \sigma}$, the Froude number $Fr_L = \frac{\dot{m}_l^2}{\rho_L^2 g D}$, the gas quality $\chi = \frac{\dot{m}_v}{\dot{m}_v + \dot{m}_l}$, and the departure from nucleate boiling $q_{DNB} = 0.131 \rho_G^{1/2} H_{lg} [g (\rho_L - \rho_G) \sigma]^{1/4}$. The two fitting functions F_1 and F_2 introduced in (9) - (11) have the form

$$F_1(q) = 646.0 \left(\frac{q}{q_{DNB}} \right)^2 + 64.8 \left(\frac{q}{q_{DNB}} \right)$$

and

$$F_2(q) = 18.8(q/q_{DNB}) + 1.023.$$

We can see that a number of the geometrical parameters of the flow has to be determined before the boundaries between the flow pattern can be calculated. These parameters include e.g. cross-sectional area of the gas flow normalized by the pipe diameter A_{gwd} , height of the liquid flow b_l , etc.. We now describe how to calculate geometrical parameters of the flow.

4.2 Geometrical parameters of the stratified flow

To find geometrical parameters of the flow one assumes usually [Bejan03] that the flow is ‘‘conceptually’’ stratified for all temperatures and flow rates, i.e. the flow cross-section has the form shown in the Fig. 8.

The following parameters of the stratified flow have to be determined (see Fig. 8). First, the stratification angle θ is found by noticing that

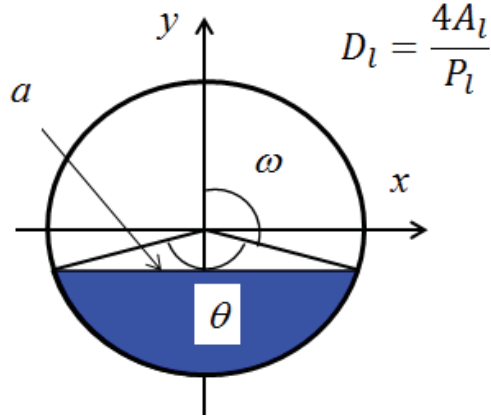


Figure 8. Geometry and parameters of the stratified flow in the pipe cross-section.

the liquid cross-section area $A_l = (1 - \alpha)A$ (shaded by blue color in the figure) is related to θ as follows

$$(1 - \alpha)A = \frac{R^2}{2}(\theta - \sin \theta).$$

Once this equation is solved with respect to θ , all other required geometrical parameters, including

- b_l - height of the liquid level,
- l_i - perimeter of the interface,
- l_{gw} - perimeter of the dry wall,
- l_{lw} - perimeter of the wetted wall,
- A_g - cross-section area of the gas,
- A_l - cross-section area of the liquid,
- S_g - dry area of the wall,
- S_l - wetted area of the wall,

are found using simple geometrical relation.

Once the equation for the θ above is solved for a given void fraction α the effective liquid level height and other geometrical parameters can be found as follows:

$$b_l = \frac{D}{2} \left(1 - \cos \left(\frac{\theta}{2} \right) \right),$$

$$l_{gw} = \frac{D}{2} (2\pi - \theta),$$

$$l_{lw} = \pi D - l_{gw},$$

$$l_i = D \sin\left(\frac{\theta}{2}\right).$$

Similar approach can be used in a more general case of the ‘‘conceptually stratified’’ flow, see e.g. [Bejan03]. The main difference is that in this case an effective height for the liquid level is determined by equating two expressions for the Lockhart-Martinelli [Lockhart49] parameter. The first expression relates Martinelli parameter to the geometrical characteristics of the flow (see [Bejan03])

$$\chi_{tt}^2 = \left[\left(\frac{l_{gwd} + l_i}{\pi} \right)^{\frac{1}{4}} \left(\frac{l_{gwd} + l_i}{A_{gwd}} + \frac{l_i}{A_{lwd}} \right) \right] \left(\frac{\pi}{l_{lwd}} \right)^{\frac{1}{4}} \frac{A_{lwd}^3}{A_{gwd}^2 l_{lwd}}. \quad (12)$$

The second expression correlates the value of the Martinelli parameter with the thermodynamic characteristics of the flow as follows

$$\chi_{tt} = \left(\frac{1 - \chi}{\chi} \right)^{.875} \left(\frac{\rho_G}{\rho_L} \right)^{.5} \left(\frac{\mu_L}{\mu_G} \right)^{.125}. \quad (13)$$

To solve the equations (12) and (13) with respect to b_l the values for the phasic cross-sections are taken in the form [Bejan03] For $b_l \leq 0.5$:

$$A_{lwd} = \frac{(8(b_l)^{.5} + 12[b_l(1 - b_l)]^{.5})}{15} \quad \text{and} \quad A_{gwd} = \frac{\pi}{4} - A_{lwd}.$$

For $b_l > 0.5$:

$$A_{gwd} = \frac{(8(1 - b_l)^{.5} + 12[b_l(1 - b_l)]^{.5})}{15} \quad \text{and} \quad A_{lwd} = \frac{\pi}{4} - A_{gwd}.$$

Here, all the geometrical parameters are made dimensionless (as indicated by additional subindex d) by scaling with the pipe diameter D or diameter square D^2 when appropriate.

Once geometrical parameters are determined one can calculate source terms as discussed in more details in the following subsection.

4.3 Heat fluxes

As a first step in the analysis of the source terms we consider heat fluxes per unit volume at the dry and wetted wall and at the interface given by the following equations written for each control volume

$$\begin{aligned} \dot{q}_{wg}^n &= H_{wg}^n (T_w^n - \tilde{T}_g^n) \frac{S_{wg}}{V}; & \dot{q}_{ig}^n &= H_{ig}^n (\tilde{T}_l^{s,n} - \tilde{T}_g^n) \frac{S_{ig}}{V}; \\ \dot{q}_{wl}^n &= H_{wl}^n (T_w^n - \tilde{T}_l^n) \frac{S_{wl}}{V}; & \dot{q}_{il}^n &= H_{il}^n (\tilde{T}_l^{s,n} - \tilde{T}_l^n) \frac{S_{il}}{V}. \end{aligned} \quad (14)$$

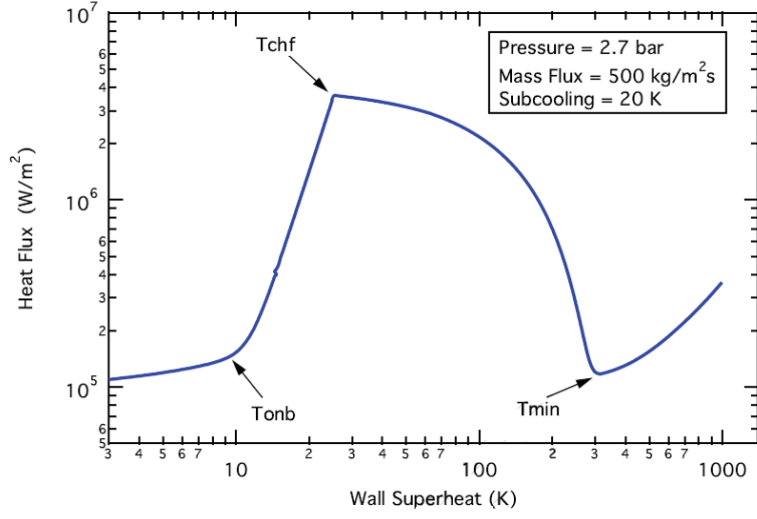


Figure 9. Boiling curve example (water-vapor) for a given pressure, mass flux, and subcooling.

An additional condition has to be imposed on these fluxes, which states that in the sum of energy equations the interface terms must sum to zero:

$$\dot{q}_{ig,L}^n + \dot{q}_{il,L}^n + \tilde{\Gamma}_{ig,L}^n (H_{ig,L}^n - H_{il,L}^n) = 0.$$

The full set of correlations required to calculate heat fluxes (14) for various flow patterns as a function of void fraction, wall superheat, and mass flux will be discussed in details in a separate report [LuchDG-III]. Here we provide a simplified discussion of the heat transfer correlations near the wall, neglecting heat fluxes at the interface. To follow the transition between various heat transfer correlations as a function of the wall superheat ΔT_{ws} ($\Delta T_{ws} = T_w - T_{sat}$) let us recall the typical shape of the boiling curve shown in the Fig. 9.

There are three characteristic temperatures that separates four regions with different physics of the heat transfer for $\Delta T_{ws} \geq 0$ (see e.g. [Bejan03, Nellis09]):

$T_{onb} > T_w \geq T_{sat}$ *Convective heat transfer*, which is characterized by complete contact of the fluid with the wall, and can be natural or forced, laminar or turbulent, single or two phase depending on the mass flow rate and mass fraction value;

$T_{chf} > T_w \geq T_{onb}$ *Nucleate boiling* that occurs when the wall temperature is above the temperature of *onset of nucleate boiling* (T_{onb}) and is characterized by bubbles nucleation, growth, and departure from the heated surface;

$T_{min} > T_w \geq T_{chf}$ *Transition boiling*, which is an intermediate regime between the nucleate boiling and film boiling regimes that occurs

when the wall temperature is above the *critical heat flux* temperature (T_{CHF}). The heat flux tends to decrease, while the dry wall area tends to increase with an increase of the superheat.

$T_w \geq T_{min}$ *Film boiling*, in which a stable layer of vapor that forms between the heated surface and the liquid, such that the bubbles form at the free interface and not at the wall. It occurs when the wall temperature is above of the Leidenfrost temperature T_{min} . The heat flux tends to grow with the increase of superheat.

The heat transfer coefficient is determined as

$$h = \frac{\kappa}{D} Nu, \quad (15)$$

where κ is thermal conductivity of the fluid, D is the pipe diameter, and Nu is the Nusselt number. The correlations are given in terms of the Nusselt number.

Convective heat transfer. In the single phase regions the following correlations for laminar and turbulent forced convection and natural convection [RELAP5-IV, TRACE]

$$Nu_c = \begin{cases} 4.36, & \text{forced (Lm) [Sellars56];} \\ 0.023 \cdot Re^{0.8} Pr^{0.4}, & \text{forced (Tb) [Dittus30];} \\ 0.1 \cdot (Gr \cdot Pr)^{1/3}, & \text{natural (Lm) [Holman89];} \\ 0.59 \cdot (Gr \cdot Pr)^{1/4}, & \text{natural (Tb) [Holman89].} \end{cases} \quad (16)$$

are chosen for the Nusselt number for both gas and liquid. To guarantee a smooth transition between the various regimes the maximum of the above numbers is taken as the value for the convective heat transfer.

Here, $Re = \frac{G \cdot D}{\mu}$ is the Reynolds number for a given flow, $Pr = \frac{\mu C_p}{\kappa}$, and $Gr = \frac{\rho^2 g \beta (T_w - T_{l(g)}) D^3}{\mu^2}$ is the Grashof number of the flow.

The convective heat flux is finally determined as follows

$$\dot{q}_c = h_c (T_w - T_l).$$

Nucleate boiling. To determine the heat flux corresponding to the nucleate boiling, one can follow e.g. [TRACE] and find first the temperature of the onset of the nucleate boiling T_{onb}

$$T_{onb} = T_l + \frac{1}{4} \left[\sqrt{\Delta T_{onb,s}} + \sqrt{\Delta T_{onb,s} + 4\Delta T_{sub}} \right]^2, \quad (17)$$

where the correction factor $F(\phi)$ as a function of the contact angle ϕ , subcool temperature ΔT_{sub} , and saturated temperature of onset of nucleate boiling $\Delta T_{onb,sat}$ are given by the following formulas

$$\Delta T_{sub} = T_{sat} - T_L; \quad \Delta T_{onb,s} = \frac{2h_{fc}\sigma T_{sat}}{F^2(\phi)\rho_g H_{lg}\kappa_l}; \quad F(\phi) = 1 - e^{-\phi^3 - 0.5\phi}.$$

Once the temperature corresponding to the onset of nucleate boiling under current flow conditions is determined the corresponding heat flux is found using the following simple correlation

$$\dot{q}_{nb} = \left[\dot{q}_c + (\dot{q}_{pb} - \dot{q}_{bi})^3 \right]^{1/3}, \quad (18)$$

where $\dot{q}_c = h_c(T_w - T_l)$ is the convective heat flux, found above, \dot{q}_{pb} is the pool boiling heat transfer, $\dot{q}_{bi} = \dot{q}_{pb}(T_{onb})$ is the pool boiling heat transfer at the onset on nucleation. To complete the calculations of the \dot{q}_{nb} we have to determine heat transfer coefficient for pool boiling using e.g. the following equation (see [TRACE])

$$h_{pb} = (h_0 \cdot F_p / q_0)^{\frac{1}{1-n}} \cdot (T_w - T_{sat})^{\frac{n}{1-n}}, \quad (19)$$

where $h_0 = 5600 [W/m^2/K]$, $q_0 = 2000 [W/m^2]$, $n = 0.9 - 0.3 \cdot Pr^{0.15}$, $F_p = 1.73 \cdot Pr^{0.27} + \left(6.1 + \frac{0.68}{1-Pr}\right) \cdot Pr^2$, $Pr = P/P_{cr}$, and P_{cr} is the pressure at critical point.

Transition boiling. Transition boiling corresponds to the intermediate regime between nucleate and film boiling. The transition boiling heat flux is usually given as a result of interpolation between characteristic heat fluxes \dot{q}_{chf} and \dot{q}_{min} . We will use the form of interpolation introduced in [TRACE]

$$\dot{q}_{tb} = f_{tb} \cdot \dot{q}_{chf} + (1 - f_{tb})\dot{q}_{min}, \quad (20)$$

where

$$f_{tb} = \left(\frac{T_w - T_{min}}{T_{chf} - T_{min}} \right)^2.$$

It can be seen from equation (20) that to find \dot{q}_{tb} one has to determine values of the four parameters: (i) \dot{q}_{chf} , (ii) \dot{q}_{min} , (iii) T_{chf} , and (iv) T_{min} .

There are a few different approaches to characterize these characteristic values. For example one could find the first two parameters using tables or correlations. Multiple correlations are available for the values of \dot{q}_{chf} and \dot{q}_{min} [Kandlikar01]. One of the best known correlations for the critical heat flux was proposed by Kutateladze [Kutateladze48]

$$\dot{q}_{chf} = K \cdot h_{lg} \rho_g \left(\frac{\sigma g (\rho_l - \rho_g)}{\rho_g^2} \right)^{1/4}. \quad (21)$$

A well known correlation for the minimum heat flux was suggested by Zuber [Zuber58]

$$\dot{q}_{min} = C \cdot h_{lg} \rho_g^{1/2} \left(\frac{\sigma g (\rho_l - \rho_g)}{(\rho_l + \rho_g)^2} \right)^{1/4}. \quad (22)$$

Coefficients K and C in the equations (21) and (22) are of the order of 0.1 for the water, but are not well known for the nitrogen [Kandlikar01, Yuan06] and can be used as fitting parameters.

Once \dot{q}_{chf} and \dot{q}_{min} are found the characteristics temperatures T_{chf} and T_{min} are calculated as follows

$$\dot{q}_{nb}(T_{chf}) = \dot{q}_{chf}, \quad \dot{q}_{fb}(T_{min}) = \dot{q}_{min}. \quad (23)$$

Alternatively, one could determine values of T_{min} and T_{chf} using correlations and then apply equations (23) to find \dot{q}_{chf} and \dot{q}_{min} .

In practice, the set of correlations is optimized by comparison of the model predictions with experimental data as will be discussed in more details in a separate technical report [LuchDG-III].

Film Boiling. To find heat flux at the wetted perimeter the film boiling heat transfer is used in the form [Bromley50]

$$h_{fb} = C \left[\frac{g \rho_g \kappa_g^2 (\rho_l - \rho_g) H_{lg} C_{pg}}{D (T_w - T_{spt}) Pr_g} \right]^{0.25},$$

where $C = 0.62$, $T_{film} = \frac{1}{2} (T_w + T_{spt})$ is film temperature and

$$H_{lg} = H_g - H_l$$

is the effective heat of vaporization. It is assumed here that all the heat transferred from the wall to the liquid through the wetted perimeter is be used to heat it up and to evaporate.

We note that the film boiling heat transfer is one of the key properties of the cryogenic flow that affect the chilldown process.

Flow corrections.

For the flow boiling the values of the characteristic heat flux \dot{q} and temperature T have to be corrected taking into account mass flux and void fraction of the flow as will be discussed in details in [LuchDG-III].

4.4 Mass fluxes

The total mass transfer per unit volume in each L -th control volume at the n -th time step $\Gamma_{g,L}^n$ is defined as a sum of interfacial mass transfer $\Gamma_{ig,L}^n$ and near wall mass transfer $\Gamma_{wg,L}^n$

$$\Gamma_{g,L}^n = \Gamma_{ig,L}^n + \Gamma_{wg,L}^n.$$

The interfacial mass transfer is given by the following relation

$$\Gamma_{ig,L}^n = \frac{\dot{q}_{il,L}^n + \dot{q}_{ig,L}^n}{H_{g*,L}^n - H_{l*,L}^n},$$

where the denominator is given by

$$H_{g*,L}^n - b_{l*,L}^n = \begin{cases} H_{gs,L}^n - H_{ls,L}^n, & \Gamma > 0; \\ H_{g,L}^n - H_{ls,L}^n, & \Gamma < 0. \end{cases}$$

The saturation values are determined using NIST tables [NIST90].

The near wall mass transfer is given e.g. by [RELAP5-IV]

$$\Gamma_{wg,L}^n = \frac{\dot{q}_{wl,L}^n}{\max\left(H_{g*,L}^n - H_{l*,L}^n, 10^4 \frac{J}{kg}\right)} M_{cor},$$

where correction coefficient M_{cor} is discussed in more details in a separate chapter related to correlations.

In the simplified version of the code we neglected the interface heat exchange in the bulk and considered only mass transfer at the wall. This simplification can be only partially justified by reasonable agreement with the experimental data during earlier chilldown stage and will be removed in the next version. As a further simplification accepted at the development stage the ambient heat transfer coefficients was taken as a constants over the whole temperature range.

Once heat and mass fluxes are found one has to determine boundary conditions at the input/output valves of the system (including dump valves) as explained in more details in the following section.

4.5 Boundary Conditions

The solution of the expanded equations (30) requires knowledge of the upwind values of the flow variables and velocities at the inlet and outlet of the system.

Thermodynamic characteristics for liquid and gas in the storage and vehicle tanks are found using separate subroutines for each tank.

Storage tank. Pressure in the storage tank is one of the main control parameters in the system and is considered as a given boundary condition. For the storage the vapor phase is assumed to be at saturation temperature corresponding to a given pressure. During loading operation the liquid in the storage tank is generally subcooled with liquid temperature being close to the equilibrium temperature at atmospheric pressure.

Vehicle tank. The vehicle tank at the KSC testbed is ventilated at all time during loading operation. And there is no back flow to the transfer line from the vehicle tank. Accordingly, the boundary condition at the exit of the transfer line is determined by the atmospheric pressure and hydrostatic pressure of the liquid in the tank.

To find gas and liquid velocities through the input and output valves one should use, in general, a two-phase flow model of the valve. Currently, for the sake of simplicity the flow of each phase through the valve is assumed to be independent and incompressible, which is reasonable approximation for gas velocities less than 50 m/sec. The void fraction of this flow through the valve is assumed to be the same as the void fraction of the incoming fluid. The resulting volumetric flow rate is

$$Q_{g(l)}^0 = K_v \sqrt{\Delta p \left(\frac{\rho_{H20}}{\rho_{g(l)}} \right)}. \quad (24)$$

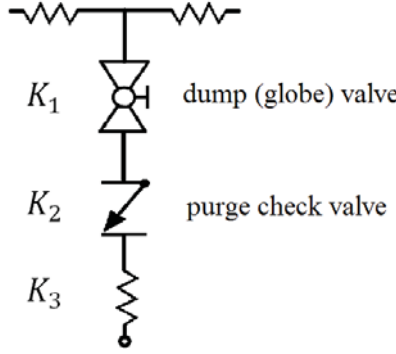


Figure 10. Schematics of the pipe with dump valve. K_1 , K_2 , and K_3 are flow coefficients for the dump valve, check valve, and other minor losses respectively.

The coupling of the pipe flow to large volumes in the storage and vehicle tanks is modeled by taking into account the inertia of the flow through the input and output valves in the form τ_{vl}

$$\dot{J}_{vl} = \frac{J_{vl}^0 - J_{vl}}{\tau_{vl}}, \quad (25)$$

where $J_{vl}^0 = Q_{g(l)}^0 \rho_{g(l)}^0$.

4.6 Dump valves model

The mass flow through the dump valves is modeled using the following simplifying assumptions: the pressure at the inlet of the dump valve can be taken as a pressure in the control volume coupled to this valve, while the pressure at the outlet of the dump valve is approximated by the atmospheric pressure. These approximations are justified by the short pipes of low resistance connecting dump valves to the transfer line and to the drain system.

The mass of the gas flow through the valves can be approximated in two different ways. In one of the approximations the flow is considered to be compressible. As a result the following equations for the mass flow rate can be used for the dump valve

$$j_{vl}^g = S_{vl} \begin{cases} \sqrt{\gamma p_g \rho_g} / \Gamma & \text{in supersonic regime} \\ \sqrt{\frac{2\gamma p_{in}}{\gamma-1} \left[\left(\frac{p_{out}}{p_{in}} \right)^{\frac{2}{\gamma}} - \left(\frac{p_{out}}{p_{in}} \right)^{\frac{\gamma+1}{\gamma}} \right]} & \text{in subsonic regime} \end{cases}$$

For relatively low gas velocities the incompressible approximation of the flow through the valve considered in the was found to be accurate enough for practically all the loading conditions at the KSC testbed. Typical configuration of the pipe with dump valve is shown in the Fig. 10.

The corresponding volumetric flow rate through the dump valve can be found as follows

$$Q_0 = \left(\frac{1}{c_1^2 K_1^2} + \frac{1}{K_2^2} + \frac{1}{K_3^2} \right)^{-1/2} \sqrt{\Delta p \cdot \frac{\rho L N^2}{\rho}},$$

where c_1 is the relative opening of the dump valve.

To take into account the inertia of the valve operation characterized by the time delay τ_V the volumetric flow rate through the dump valve was modeled in the following form

$$\dot{Q} = \frac{Q_0 - Q}{\tau_V}.$$

The heat flux through the dump valve H_{dv} was then calculated as

$$H_{dv} = Q \rho_g c_p T_g,$$

where $c_p T_g$ is the gas enthalpy in the control volume attached to the dump valve.

Once the boundary conditions including heat and mass fluxes at the liquid/gas/wall interfaces and through the input/output valves are found the algorithm proceeds to the calculations of the first integration step.

5 First step

The first integration step of the algorithm includes the following sub-steps:

1. Solve expanded equation with respect to pressure in terms of new velocities;
2. Substitute this solution into momenta equations and solve resulting block tri-diagonal matrix equation for the new velocities;
3. Find new pressure;
4. Find provisional values for the energies and void fractions using expanded equations;
5. Find provisional values for mass and heat fluxes.

We now discuss in more details each of the sub-steps.

5.1 Expanded equations

The set of expanded conservation equations discretized on the main grid (see Sec. 2.2) include:

the sum density equation

$$\begin{aligned} & \alpha_{g,L}^n d\rho_{g,L}^{n+1} + \beta_{l,L}^n d\rho_{l,L}^{n+1} + d\alpha_{g,L}^{n+1} (\rho_{g,L}^n - \rho_{l,L}^n) + \\ & \frac{\Delta t}{V} \left((\overline{\alpha\rho A})_{g,j+1}^n u_{g,j+1}^{n+1} - (\overline{\alpha\rho A})_{g,j}^n u_{g,j}^{n+1} \right) + \\ & \frac{\Delta t}{V} \left((\overline{\alpha\rho A})_{l,j+1}^n u_{l,j+1}^{n+1} - (\overline{\alpha\rho A})_{l,j}^n u_{l,j}^{n+1} \right) = 0, \end{aligned} \quad (26)$$

the difference density equation

$$\begin{aligned} & \alpha_{g,L}^n d\rho_{g,L}^{n+1} - \beta_{l,L}^n d\rho_{l,L}^{n+1} + d\alpha_{g,L}^{n+1} (\rho_{g,L}^n + \rho_{l,L}^n) + \\ & \frac{\Delta t}{V} \left((\overline{\alpha\rho A})_{g,j+1}^n u_{g,j+1}^{n+1} - (\overline{\alpha\rho A})_{g,j}^n u_{g,j}^{n+1} \right) - \\ & \frac{\Delta t}{V} \left((\overline{\alpha\rho A})_{l,j+1}^n u_{l,j+1}^{n+1} - (\overline{\alpha\rho A})_{l,j}^n u_{l,j}^{n+1} \right) = 2\Gamma_{g,L}^n, \end{aligned} \quad (27)$$

the gas energy equation

$$\begin{aligned} & (\rho_{g,L}^n e_{g,L}^n + p_L^n) d\alpha_{g,L}^{n+1} + (\alpha\rho)_{g,L}^n de_{g,L}^{n+1} + (\alpha e)_{g,L}^n d\rho_{g,L}^{n+1} + \\ & \frac{\Delta t}{V} \left[(A\bar{\alpha}(\bar{\rho e} + p))_{g,j+1}^n u_{g,j+1}^{n+1} + (A\bar{\alpha}(\bar{\rho e} + p))_{g,j}^n u_{g,j}^{n+1} \right] = \\ & \left[H_{gw,L}^n (T_{w,L}^n - \tilde{T}_{g,L}^{n+1}) S_{wg} + H_{ig,L}^n (\tilde{T}_{l,L}^{s,n+1} - \tilde{T}_{g,L}^{n+1}) S_{ig} \right. \\ & \left. + \tilde{\Gamma}_{ig,L}^n H_{ig,L}^n + \tilde{\Gamma}_{wg,L}^n H_{wg,L}^n \right] \frac{\Delta t}{V}, \end{aligned} \quad (28)$$

the liquid energy equation

$$\begin{aligned} & -(\rho_{l,L}^n e_{l,L}^n + p_L^n) d\alpha_{g,L}^{n+1} + (\alpha\rho)_{l,L}^n de_{l,L}^{n+1} + (\alpha e)_{l,L}^n d\rho_{l,L}^{n+1} + \\ & \frac{\Delta t}{V} \left[(A\bar{\alpha}(\bar{\rho e} + p))_{l,j+1}^n u_{l,j+1}^{n+1} + (A\bar{\alpha}(\bar{\rho e} + p))_{l,j}^n u_{l,j}^{n+1} \right] = \\ & \left[H_{lw,L}^n (T_{w,L}^n - \tilde{T}_{l,L}^{n+1}) S_{wl} + H_{il,L}^n (\tilde{T}_{l,L}^{s,n+1} - \tilde{T}_{l,L}^{n+1}) S_{il} \right. \\ & \left. - \tilde{\Gamma}_{ig,L}^n H_{il,L}^n - \tilde{\Gamma}_{wg,L}^n H_{wl,L}^n \right] \frac{\Delta t}{V}. \end{aligned} \quad (29)$$

5.1.1 Solving expanded equations with respect to pressure

The four coupled equations (26) - (29) for the sum and difference density and for the gas and liquid energy can be rewritten in matrix form

$$A_x^n \begin{bmatrix} d\alpha_g \\ de_g \\ de_l \\ dp \end{bmatrix}_L^{n+1} = a_x^n du_{g,j+1}^{n+1} + b_x^n du_{g,j}^{n+1} + c_x^n du_{l,j+1}^{n+1} + d_x^n du_{l,j}^{n+1} + e_x^n, \quad (30)$$

Here the vector of unknowns $dx_L^{n+1} = \{d\alpha_{g,L}^{n+1}, de_{g,L}^{n+1}, de_{l,L}^{n+1}, dp_L^{n+1}\}$.

Assuming for now old values of the temperature on the right hand side of eqs. (26) - (29) and using the following expansion for the densities

$$\begin{aligned} d\rho_{g,L}^{n+1} &= \rho_{g,L}^{n+1} - \rho_{g,L}^n \approx \left(\frac{\partial \rho}{\partial p} \right)_{g,L}^n dp_L^{n+1} + \left(\frac{\partial \rho}{\partial e} \right)_{g,L}^n de_{g,L}^{n+1}; \\ d\rho_{l,L}^{n+1} &= \rho_{l,L}^{n+1} - \rho_{l,L}^n \approx \left(\frac{\partial \rho}{\partial p} \right)_{l,L}^n dp_L^{n+1} + \left(\frac{\partial \rho}{\partial e} \right)_{l,L}^n de_{l,L}^{n+1}; \end{aligned}$$

the elements of the matrix A_x^n can be written in the following form (index (j) enumerates columns of the matrix A_x^n)

$$A_x^{(1)} = \begin{bmatrix} \alpha_{g,L}^n (\partial_e \rho)_{g,L}^n \\ \alpha_{g,L}^n \left((e \partial_e \rho)_{g,L}^n + \rho_{g,L}^n \right) \\ 0 \\ \alpha_{g,L}^n (\partial_e \rho)_{g,L}^n \end{bmatrix}; \quad A_x^{(2)} = \begin{bmatrix} -\beta_{g,L}^n (\partial_e \rho)_{l,L}^n \\ 0 \\ \beta_{g,L}^n \left(\rho_{l,L}^n + (e \partial_e \rho)_{l,L}^n \right) \\ \beta_{g,L}^n (\partial_e \rho)_{l,L}^n \end{bmatrix}$$

$$A_x^{(3)} = \begin{bmatrix} \rho_{g,L}^n + \rho_{l,L}^n \\ (e \rho)_{g,L}^n + p_L^n \\ -(e \rho)_{l,L}^n - p_L^n \\ \rho_{g,L}^n - \rho_{l,L}^n \end{bmatrix}; \quad A_x^{(4)} = \begin{bmatrix} \alpha_{g,L}^n (\partial_p \rho)_{g,L}^n - \beta_{g,L}^n (\partial_p \rho)_{l,L}^n \\ (e \alpha \partial_p \rho)_{g,L}^n \\ (\beta e \partial_p \rho)_{l,L}^n \\ \alpha_{g,L}^n (\partial_p \rho)_{g,L}^n + \beta_{g,L}^n (\partial_p \rho)_{l,L}^n \end{bmatrix}$$

Columns of the vector-multipliers for gas velocities on the right hand side of the eq. (30) have the form

$$a_x^n = - \begin{bmatrix} \widehat{\rho}_{g,j+1}^n \\ (\widehat{e \rho})_{g,j+1}^n + p_L^n \\ 0 \\ \widehat{\rho}_{g,j+1}^n \end{bmatrix} \cdot n_{g,j+1}^n; \quad b_x^n = \begin{bmatrix} \widehat{\rho}_{g,j}^n \\ (\widehat{e \rho})_{g,j}^n + p_L^n \\ 0 \\ \widehat{\rho}_{g,j}^n \end{bmatrix} \cdot n_{g,j}^n;$$

Vector-columns for the liquid velocities are

$$c_x^n = \begin{bmatrix} \widehat{\rho}_{l,j+1}^n \\ 0 \\ -(\widehat{e \rho})_{l,j+1}^n - p_L^n \\ -\widehat{\rho}_{l,j+1}^n \end{bmatrix} \cdot n_{l,j+1}^n; \quad d_x^n = \begin{bmatrix} -\widehat{\rho}_{l,j}^n \\ 0 \\ (\widehat{e \rho})_{l,j}^n + p_L^n \\ \widehat{\rho}_{l,j}^n \end{bmatrix} \cdot n_{l,j}^n,$$

where the coefficients $n_{i,j}^n$ are of the form

$$n_{g,j}^n = \widehat{\alpha}_{g,j}^n \frac{\Delta t A_j}{V_L}; \quad n_{l,j}^n = \widehat{\alpha}_{l,j}^n \frac{\Delta t A_j}{V_L}.$$

Finally, the free vector in eq. (30) is written as follows

$$e_x^n = \begin{bmatrix} 2\Gamma_{g,L}^n V_L \\ \Gamma_{g,L}^n H_{wg}^n V_L - Q_{wg} \\ -\Gamma_{g,L}^n H_{wl}^n V_L - Q_{wl} \\ 0 \end{bmatrix} \cdot \frac{\Delta t}{V_L} + a_x^n u_{g,j+1}^n + b_x^n u_{g,j}^n + c_x^n u_{l,j+1}^n + d_x^n u_{l,j}^n$$

The matrix equation (30) is solved with respect to dp_L^{n+1} in terms of new velocities $du_{g,j+1}^{n+1}$, $du_{g,j}^{n+1}$, $du_{l,j+1}^{n+1}$, $du_{l,j}^{n+1}$.

The new pressure dp_L^{n+1} is expressed in terms of new velocities $du_{g,j+1}^{n+1}$, $du_{g,j}^{n+1}$, $du_{l,j+1}^{n+1}$, $du_{l,j}^{n+1}$ using the last row of eq. (30) multiplied by the inverted matrix A_x^n

$$dp_L^{n+1} = (A_x^n)^{-1} \left(a_x^n du_{g,j+1}^{n+1} + b_x^n du_{g,j}^{n+1} + c_x^n du_{l,j+1}^{n+1} + d_x^n du_{l,j}^{n+1} + e_x^n \right) \quad (31)$$

where $(A_x^n)_4^{-1}$ is the 4-th row of the inverted matrix A_x .

We note that excursive numerical tests has revealed the high sensitivity of the code to the accuracy of numerical inversion of the matrix A_x^n . This is due to stiffness of the problem. Indeed, the eigavalues of the matrix A_x^n are different by twelve orders of the magnitude. As a result the errors of numerical inversion of matrix A_x^n cause significant stability and accuracy problem. To solve this problem we used the exact equations for the elements of the matrix $(A_x^n)^{-1}$ in the code. Such a simple solution sufficed to improve the stability and accuracy and also allowed to speed up the calculations.

To build matrix A_x^n and vectors a_x^n , b_x^n , c_x^n , d_x^n , and e_x^n ones has to calculate

- upwind values for void fraction, energy, and density,
- density derivatives with respect to pressure and energy,
- source terms, i.e. right hand sides of eqs. (26)-(29).

The analysis of the heat and mass fluxes required for the calculations of the source terms was given in the Sections 4.3 and 4.4. Below we define the upwind values and discuss calculations of the density derivatives. Note, that in the current version of the code the temperatures in the right hand sides of the energy equations (28) and (29) are taken at the previous time step to simplify the calculations.

5.1.2 Upwind values

The values of the velocities, mass, energy, and void fractions are calculated at the interfaces centered at staggered grid with indexes $j = 1, \dots, N + 1$. The values of scalar variables are calculated using upwind scheme following [RELAP5-1]. For the density we use

$$\hat{\varphi}_j = \frac{1}{2}(\varphi_{L-1} + \varphi_L) + \frac{1}{2}(s_{u,j} + z_{u,j} \cdot s_{p,j})(\varphi_{L-1} - \varphi_L) = \frac{\varphi_{L-1}}{2} + (1 - (s_{u,j} + z_{u,j} \cdot s_{p,j})) \frac{\varphi_L}{2}, \quad (32)$$

For the energy and void fraction we use

$$\begin{aligned} \hat{\psi}_j = & \frac{1}{2}(\psi_{L-1} + \psi_L) + \frac{1}{2}(s_{u,j} + z_{u,j} \cdot s_{p,j})(\psi_{L-1} - \psi_L) + \\ & z_{u,j} \cdot z_{p,j} \left(-\frac{1}{2}(\psi_{L-1} + \psi_L) + \frac{(\psi_{L-1}\rho_{g(L),L-1} + \psi_L\rho_{g(L),L})}{\rho_{g(L),L-1} + \rho_{g(L),L}} \right) = \\ & \left(1 + (s_{u,j} + z_{u,j} \cdot s_{p,j}) - z_{u,j} \cdot z_{p,j} + \frac{2\rho_{g(L),L-1}}{\rho_{g(L),L-1} + \rho_{g(L),L}} \right) \frac{\psi_{L-1}}{2} + \\ & \left(1 - (s_{u,j} + z_{u,j} \cdot s_{p,j}) - z_{u,j} \cdot z_{p,j} + \frac{2\rho_{g(L),L-1}}{\rho_{g(L),L-1} + \rho_{g(L),L}} \right) \frac{\psi_L}{2}. \end{aligned} \quad (33)$$

Here the following notations are introduced

$$\begin{aligned} s_{u,j} &= \text{sign}(u_j); & z_{u,j} &= \{1 \text{ if } u_j = 0, 0 \text{ otherwise}\}; \\ s_{p,j} &= \text{sign}(p_j); & z_{p,j} &= \{1 \text{ if } p_j = 0, 0 \text{ otherwise}\}. \end{aligned}$$

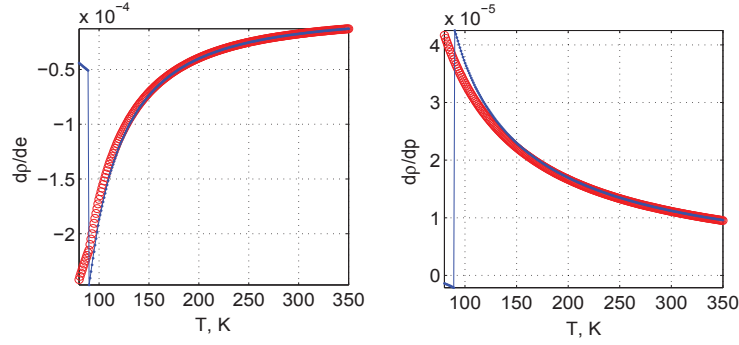


Figure 11. Comparison of the values for the density derivatives obtained using ideal gas equations (red circles) and [Bridgman61] equations (blue dots).

It is also recommended (see [RELAP5-I]) to use additional smoothing for small mixture velocity $j_m = \hat{\alpha}_{g,j}u_{g,j} + \hat{\alpha}_{l,j}u_{l,j}$ in the form

$$\varphi_j = \zeta_j \varphi_{L-1} + (1 - \zeta_j) \varphi_L; \quad \zeta_j = \begin{cases} 1 & \text{when } j_m > j_{lim} \\ \xi^2 (3 - 2\xi) & \text{when } -j_{lim} < j_m < j_{lim} \\ 0 & \text{when } j_m < -j_{lim} \end{cases},$$

where $\xi = \frac{j_m + j_{lim}}{2j_{lim}}$ and $j_{lim} = 0.46$ m/s. In the present version of the code this smoothing was omitted to simplify the calculations.

5.1.3 Density derivatives

In the present version of the code the temperatures in the source terms are taken at old time. Therefore, only density derivatives have to be calculated. Density derivatives are found using two-dimensional interpolation of NIST tables [NIST90]. The required values of the $\frac{\partial \rho}{\partial p}[T]$ could be taken directly from the tables. In more general case the derivatives were estimated using the following equations [Bridgman61]

$$\left(\frac{\partial \rho}{\partial e}\right)_p = -\frac{\rho \beta}{\left(c_p - \frac{\beta p}{\rho}\right)}; \quad \left(\frac{\partial \rho}{\partial p}\right)_U = \frac{c_p \kappa \rho - T \beta^2}{\left(c_p - \beta p / \rho\right)}$$

In addition, at the development stage the density derivatives for the gas phase were frequently approximated using ideal gas equations

$$\left(\frac{\partial \rho}{\partial e}\right)_p = -\left(\frac{\rho}{e_g}\right); \quad \left(\frac{\partial \rho}{\partial p}\right)_U = \frac{1}{(\gamma - 1)e_g}.$$

The use of ideal gas approximation can be justified by direct comparison of the derivatives values obtained using [Bridgman61] equations and ideal gas equations as shown in the Fig. 11. It can be seen that ideal

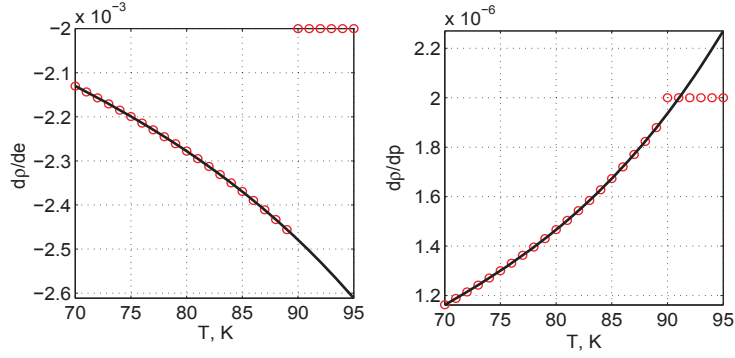


Figure 12. Comparison of the values for the density derivatives obtained using table data (red circles) and polynomial approximation (black solid lines).

gas equations approximate table values with reasonable accuracy all the way down to the temperatures around 100 K.

For density derivatives in the liquid phase simple polynomial approximations can be used as shown in the Fig. 12

We note that for any type of approximation a special care has to be taken to avoid singularities at critical temperature.

5.2 Momentum equations

One of the critical steps of the nearly-implicit algorithm that determines its accuracy and speed is the solution of the velocity matrix, which we will discuss now in more details.

The original non-conservative version of the gas momentum conservation equation for the Wallis model has the following form (see (1) and (2), cf [Staedtke], [Wallis69]) for the gas

$$A\alpha\rho_g u_{g,x} + \frac{1}{2}A\alpha\rho_g (u_g^2)_{,x} + A\alpha p_{,x} = -A\alpha\rho_g z_{,x} - \left(\frac{f_{glwg}}{4}\right) \frac{\rho_g u_g |u_g|}{2} - c_i u_R |u_R| + A\Gamma_g (u_{gi} - u_g) + M_V \quad (34)$$

and for the liquid momentum conservation equation

$$A\beta\rho_l u_{l,x} + \frac{1}{2}A\beta\rho_l (u_l^2)_{,x} + A\beta p_{,x} = -A\beta\rho_l z_{,x} - \left(\frac{f_{llwl}}{4}\right) \frac{\rho_l u_l |u_l|}{2} - c_i u_R |u_R| - A\Gamma_g (u_{li} - u_l) - M_V. \quad (35)$$

Here M_V is the virtual mass term

$$M_V = C\alpha(1-\alpha)\rho_m \left[\frac{\partial(u_g - u_l)}{\partial t} + u_l \frac{\partial u_g}{\partial x} - u_g \frac{\partial u_l}{\partial x} \right], \quad (36)$$

and ρ_m is the mixture density

$$\rho_m = \alpha_g \rho_g + \alpha_l \rho_l.$$

5.2.1 Numerically convenient form

To enhance the stability of integration in semi-implicit and nearly-implicit algorithms we follow recommendations of the RELAP5 code and use instead of the original equations (34) and (35) the sum

$$\begin{aligned} \alpha\rho_g u_{g,t} + \beta\rho_l u_{l,t} + \frac{\alpha\rho_g}{2}(u_g^2)_{,x} + \frac{\beta\rho_l}{2}(u_l^2)_{,x} + p_{,x} = -\rho_m z_{,x} - \\ \alpha\rho_g u_g F_{wg} - \beta\rho_l u_l F_{wl} - \Gamma_g (u_g - u_l), \end{aligned} \quad (37)$$

and difference momenta equations

$$\begin{aligned} u_{g,t} - u_{l,t} + \frac{(u_g^2)_{,x}}{2} + \frac{(u_l^2)_{,x}}{2} + \left(\frac{1}{\rho_g} + \frac{1}{\rho_l}\right) p_{,x} = u_l F_{wl} - u_g F_{wg} + \\ \frac{\Gamma_g}{\alpha\rho_g} (u_i - u_g) + \frac{\Gamma_g}{\beta\rho_l} (u_i - u_l) + \rho_m F_i (u_g - u_l) + \frac{\rho_m}{\alpha\rho_g\beta\rho_l} \tilde{M}_V \end{aligned} \quad (38)$$

The following simplifying notations were introduced for the wall friction (cf [RELAP5-I])

$$A\alpha_g\rho_g u_g F_{wg} = f_g l_{wg} \frac{\rho_g u_g |u_g|}{2}, \quad A\alpha_l\rho_l u_l F_{wl} = f_l l_{wl} \frac{\rho_l u_l |u_l|}{2}. \quad (39)$$

Similarly for the interfacial friction we have

$$A\alpha\rho_g F_{ig} (u_g - u_l) = A(1 - \alpha) \rho_l u_l F_{il} (u_g - u_l) = c_{gi} u_R |u_R|$$

Note that in writing sum and difference momenta equations the original equations were divided by cross-sectional area A . In addition, in deriving the difference momenta equation the original equations were divided by the product of void fraction and density for each phase. Note also, that difference equation involves reduced virtual mass term \tilde{M}_V , which excludes spatial derivatives in (36).

In the nearly-implicit algorithm the kinetic energy terms are treated approximately implicitly as follows

$$\begin{aligned} (u_g^2)_L^{n+1} = (u_{g,L}^{n+1} - u_{g,L}^n)^2 + 2u_{g,L}^{n+1} u_{g,L}^n - (u_{g,L}^n)^2 \approx \\ 2u_{g,L}^{n+1} u_{g,L}^n - 2(u_{g,L}^n)^2 + (u_{g,L}^n)^2 = 2du_{g,L}^{n+1} u_{g,L}^n + (u_{g,L}^n)^2 \end{aligned}$$

The resulting finite-difference momentum equations for one control volume on the staggered grid can now be re-written for the sum (40)

$$\begin{aligned} \left[(\bar{\alpha}\rho)_{g,j}^n du_{g,j}^{n+1} + (\bar{\alpha}\rho)_{l,j}^n du_{l,j}^{n+1} \right] \Delta x_j + \\ \frac{\Delta t}{2} (\bar{\alpha}\rho)_{g,j}^n \left(2du_{g,L}^{n+1} u_{g,L}^n + u_{g,L}^{n,2} - 2du_{g,L-1}^{n+1} u_{g,L}^n - u_{g,L-1}^{n,2} \right) + \\ \frac{\Delta t}{2} (\bar{\alpha}\rho)_{l,j}^n \left(2du_{l,L}^{n+1} u_{l,L}^n + u_{l,L}^{n,2} - 2du_{l,L-1}^{n+1} u_{l,L}^n - u_{l,L-1}^{n,2} \right) = \\ - \left(dp_L^{n+1} - dp_{L-1}^{n+1} \right) \Delta t - \left(p_L^n - p_{L-1}^n \right) \Delta t - \\ \Delta t \Delta x_j \left[\rho_{m,j}^n g \Delta z_j + (\bar{\alpha}\rho)_{g,j}^n F_{wg,j}^n \left(du_{g,j}^{n+1} + u_{g,j}^n \right) + \right. \\ \left. (\bar{\alpha}\rho)_{l,j}^n F_{wl,j}^n \left(du_{l,j}^{n+1} + u_{l,j}^n \right) - \Gamma_{g,j}^n \left(du_{g,j}^{n+1} + u_{g,j}^n - du_{l,j}^{n+1} - u_{l,j}^n \right) \right] \end{aligned} \quad (40)$$

and for the difference (41)

$$\begin{aligned}
& \left(1 + \frac{c\rho_m^2}{\bar{\rho}_g\bar{\rho}_l}\right)_j^n \left[du_{g,j}^{n+1} - du_{l,j}^{n+1}\right] \Delta x_j + \\
& \frac{\Delta t}{2} \left(\frac{\tilde{\alpha}\rho}{\bar{\alpha}\rho}\right)_{g,j}^n \left(2du_{g,L}^{n+1}u_{g,L}^n + u_{g,L}^{n,2} - 2du_{g,L-1}^{n+1}u_{g,L}^n - u_{g,L-1}^{n,2}\right) - \\
& \left(\frac{\tilde{\alpha}\rho}{\bar{\alpha}\rho}\right)_{l,j}^n \left(2du_{l,L}^{n+1}u_{l,L}^n + u_{l,L}^{n,2} - 2du_{l,L-1}^{n+1}u_{l,L}^n - u_{l,L-1}^{n,2}\right) = \\
& - \left(\frac{\bar{\rho}_l - \bar{\rho}_g}{\bar{\rho}_l\bar{\rho}_g}\right) \left(p_L^{n+1} - p_{L-1}^{n+1}\right) \Delta t - \left\{F_{wg,j}^n \left(du_{g,j}^{n+1} + u_{g,j}^n\right) - \right. \\
& F_{wl,j}^n \left(du_{l,j}^{n+1} + u_{l,j}^n\right) - \Gamma_{g,j}^n \frac{\rho_{m,j}^n du_{l,j}^{n+1} - (\bar{\alpha}\rho)_{g,j}^n du_{l,j}^{n+1} - (\bar{\alpha}\rho)_{l,j}^n du_{g,j}^{n+1}}{(\bar{\alpha}\rho)_{g,j}^n (\bar{\alpha}\rho)_{l,j}^n} - \\
& \Gamma_{g,j}^n \frac{\rho_{m,j}^n u_{l,j}^n - (\bar{\alpha}\rho)_{g,j}^n u_{l,j}^n - (\bar{\alpha}\rho)_{l,j}^n u_{g,j}^n}{(\bar{\alpha}\rho)_{g,j}^n (\bar{\alpha}\rho)_{l,j}^n} \times \\
& \left. (F_I\rho)_j^n \left(du_{g,j}^{n+1} + u_{g,j}^n - du_{l,j}^{n+1} - u_{l,j}^n\right)\right\} \Delta t \Delta x_j
\end{aligned} \tag{41}$$

of momenta equations.

The matrix form of the last two equations reads

$$\begin{aligned}
B_u^n \begin{bmatrix} du \\ dv \end{bmatrix}_{j-1}^{n+1} + C_u^n \begin{bmatrix} du \\ dv \end{bmatrix}_j^{n+1} + D_u^n \begin{bmatrix} du \\ dv \end{bmatrix}_{j+1}^{n+1} = \\
b_0 + b_1 dp_L^{n+1} + b_2 dp_{L-1}^{n+1}
\end{aligned} \tag{42}$$

It can be noticed that the relations between the new velocities is non-local for the two main reasons. Firstly, it involves velocities at faces $\{j-1, j, j+1\}$. Secondly, it depends on new volume centered velocities $u_{g,k}$ and momenta p_k at locations $\{L, L-1\}$.

In turn, volume centered pressures and velocities are related to the face centered velocities at the neighboring cells. This relation for the pressures was obtained earlier (see eq. (31)) and is repeated here in a more compact form

$$dp_L^{n+1} = a_p^L du_{g,j+1}^{n+1} + b_p^L du_{g,j}^{n+1} + c_p^L du_{l,j+1}^{n+1} + d_p^L du_{l,j}^{n+1} + e_p^L, \tag{43}$$

where coefficients on the right hand side are $a_p = (A_x^n)_4^{-1} a_x^n$, $b_p = (A_x^n)_4^{-1} b_x^n$, $c_p = (A_x^n)_4^{-1} c_x^n$, $d_p = (A_x^n)_4^{-1} d_x^n$, and $e_p = (A_x^n)_4^{-1} e_x^n$.

The corresponding relation for the volume centered velocities $du_{g(l),L}^{n+1}$ in terms of the velocities at the faces is given in the next section.

5.2.2 The volume-centered velocities

The volume-centered velocities can be in general represented in the form

$$u_{g(l),L} = a_{g(l),L} u_{g(l),j+1} + b_{g(l),L} u_{g(l),j} \tag{44}$$

For example for a straight section of the pipe we have

$$u_{g(l),L} = \frac{A_j \widehat{\alpha}_{g(l),j} \widehat{\rho}_{g(l),j}}{2A_L \alpha_{g(l),L} \rho_{g(l),L}} u_{g(l),j} + \frac{A_{j+1} \widehat{\alpha}_{g(l),j+1} \widehat{\rho}_{g(l),j+1}}{2A_L \alpha_{g(l),L} \rho_{g(l),L}} u_{g(l),j+1}. \tag{45}$$

$$\begin{aligned}
a_{k,21}^n &= \left(\left(\frac{\tilde{\alpha}\rho}{\alpha\rho} \right)_{g,j}^n b_{g,L-1} u_{g,L-1}^n - \left(\frac{\tilde{\rho}_l - \tilde{\rho}_g}{\rho_l \rho_g} \right) a_{p2,L-1} \right) \Delta t; \\
a_{k,22}^n &= \left(\left(\frac{\tilde{\alpha}\rho}{\alpha\rho} \right)_{l,j}^n b_{l,L-1} u_{l,L-1}^n - \left(\frac{\tilde{\rho}_l - \tilde{\rho}_g}{\rho_l \rho_g} \right) a_{p4,L-1} \right) \Delta t.
\end{aligned}$$

For the coefficients of the B_i matrix we have

$$\begin{aligned}
b_{k,11}^n &= \left(\left((\tilde{\alpha}\rho)_{g,j}^n (1 + F_{wg,j}^n) + \Gamma_{g,j}^n \right) \Delta x_j + \right. \\
&\quad \left. (\tilde{\alpha}\rho)_{g,j}^n (b_{g,L} u_{g,L}^n - a_{g,L-1} u_{g,L-1}^n) + (a_{p2,L} - a_{p1,L-1}) \right) \Delta t; \\
b_{k,12}^n &= \left(\left((\tilde{\alpha}\rho)_{l,j}^n (1 + F_{wl,j}^n) - \Gamma_{g,j}^n \right) \Delta x_j + \right. \\
&\quad \left. (\tilde{\alpha}\rho)_{l,j}^n (b_{l,L} u_{l,L}^n - a_{l,L-1} u_{l,L-1}^n) + (a_{p4,L} - a_{p3,L-1}) \right) \Delta t; \\
b_{k,21}^n &= \left(1 + \frac{c(\tilde{\rho}_m^n)^2}{\tilde{\rho}_g^n \tilde{\rho}_l^n} \right)_j \Delta x_j + \Delta t \left(\frac{\tilde{\alpha}\rho}{\alpha\rho} \right)_{g,j}^n (b_{g,L} u_{g,L}^n - a_{l,L-1} u_{l,L-1}^n) \\
&\quad + F_{wg,j}^n \Delta x_j \Delta t - \frac{\Gamma_{g,j}^n}{(\tilde{\alpha}\rho)_{g,j}^n} \left(\frac{\lambda_j^n \tilde{\rho}_m^n}{(\tilde{\alpha}\rho)_{l,j}^n} - 1 \right) \Delta x_j \Delta t \\
&\quad + \left(\frac{\tilde{\rho}_l - \tilde{\rho}_g}{\rho_l \rho_g} \right) (a_{p2,L} - a_{p1,L-1}) \Delta t + \tilde{\rho}_{m,j}^n F_{i,j}^n \Delta x_j \Delta t; \\
b_{k,22}^n &= - \left(1 + \frac{c(\tilde{\rho}_m^n)^2}{\tilde{\rho}_g^n \tilde{\rho}_l^n} \right)_j \Delta x_j - \Delta t \left(\frac{\tilde{\alpha}\rho}{\alpha\rho} \right)_{l,j}^n (b_{l,L} u_{l,L}^n - a_{l,L-1} u_{l,L-1}^n) - \\
&\quad F_{wl,j}^n \Delta x_j \Delta t - \frac{\Gamma_{g,j}^n}{(\tilde{\alpha}\rho)_{l,j}^n} \left(\frac{(1-\lambda_j^n) \tilde{\rho}_m^n}{(\tilde{\alpha}\rho)_{g,j}^n} - 1 \right) \Delta x_j \Delta t + \\
&\quad \left(\frac{\tilde{\rho}_l - \tilde{\rho}_g}{\rho_l \rho_g} \right) (a_{p4,L} - a_{p3,L-1}) \Delta t - \tilde{\rho}_{m,j}^n F_{i,j}^n \Delta x_j \Delta t;
\end{aligned} \tag{48}$$

For the coefficients of C_i matrices we have

$$\begin{aligned}
c_{k,11}^n &= \left((\tilde{\alpha}\rho)_{g,j}^n a_{g,L} u_{g,L}^n + a_{p1,L} \right) \Delta t; \\
c_{k,12}^n &= \left((\tilde{\alpha}\rho)_{l,j}^n a_{l,L} u_{l,L}^n + a_{p3,L} \right) \Delta t; \\
c_{k,21}^n &= \left(\left(\frac{\tilde{\alpha}\rho}{\alpha\rho} \right)_{g,j}^n a_{g,L} u_{g,L}^n + \left(\frac{\tilde{\rho}_l - \tilde{\rho}_g}{\rho_l \rho_g} \right) a_{p1,L} \right) \Delta t; \\
c_{k,22}^n &= \left(- \left(\frac{\tilde{\alpha}\rho}{\alpha\rho} \right)_{g,j}^n a_{l,L} u_{l,L}^n + \left(\frac{\tilde{\rho}_l - \tilde{\rho}_g}{\rho_l \rho_g} \right) a_{p3,L} \right) \Delta t.
\end{aligned} \tag{49}$$

The free vector has the form

$$\begin{aligned}
n_{2k}^n &= \tilde{\rho}_{m,j}^n g \left(\frac{\tilde{\rho}_l - \tilde{\rho}_g}{\rho_l \rho_g} \right) \Delta y_L^n \Delta t - \frac{(\tilde{\alpha}\rho)_{g,j}^n}{2} \left((u_{g,L}^n)^2 - (u_{g,L-1}^n)^2 \right) \Delta t + \\
&\quad \frac{(\tilde{\alpha}\rho)_{l,j}^n}{2} \left((u_{l,L}^n)^2 - (u_{l,L-1}^n)^2 \right) \Delta t + \left[\frac{\Gamma_{g,j}^n \tilde{\rho}_m^n}{(\tilde{\alpha}\rho)_{g,j}^n (\tilde{\alpha}\rho)_{l,j}^n} \times \right. \\
&\quad \left. \left(\lambda_j^n u_{g,j}^n - (1 - \lambda_j^n) u_{l,j}^n \right) - \frac{\Gamma_{g,j}^n}{(\tilde{\alpha}\rho)_{g,j}^n} u_{g,j}^n - \frac{\Gamma_{g,j}^n}{(\tilde{\alpha}\rho)_{l,j}^n} u_{l,j}^n \right] \Delta x_j \Delta t - \\
&\quad \left(F_{wg,j}^n u_{g,j}^n - F_{wl,j}^n u_{l,j}^n \right) \Delta x_j \Delta t - \left(\frac{\tilde{\rho}_l - \tilde{\rho}_g}{\rho_l \rho_g} \right) \times \\
&\quad \left(p_L^n - p_{L-1}^n + a_{p5,L}^n - a_{p5,L-1}^n \right) \Delta t - \tilde{\rho}_{m,j}^n F_{i,j}^n (u_{g,j}^n - u_{l,j}^n) \Delta x_j \Delta t; \\
n_{2k+1}^n &= - \left(-\tilde{\rho}_{m,j}^n g \Delta z_j + (\tilde{\alpha}\rho)_{g,j}^n F_{wg,j}^n u_{g,j}^n + (\tilde{\alpha}\rho)_{l,j}^n F_{wl,j}^n u_{l,j}^n + \right. \\
&\quad \left. \Gamma_{g,j}^n (u_{g,j}^n - u_{l,j}^n) \right) \Delta x_j \Delta t - \frac{(\tilde{\alpha}\rho)_{g,j}^n}{2} \left((u_{g,L}^n)^2 - (u_{g,L-1}^n)^2 \right) \Delta t - \\
&\quad \frac{(\tilde{\alpha}\rho)_{l,j}^n}{2} \left((u_{l,L}^n)^2 - (u_{l,L-1}^n)^2 \right) \Delta t - \left(p_L^n - p_{L-1}^n + a_{p5,L}^n - a_{p5,L-1}^n \right) \Delta t.
\end{aligned} \tag{50}$$

Many methods exist that solve block tridiagonal equations of the form (46). We are specifically interested in the extension of the Thomas algorithm [Reimar66], which allows to use the fact that our matrices have size (2×2) and inversion and multiplication of the matrices can be explicitly coded. In [Reimar66] it is demonstrated that a simple forward elimination-backward substitution is successful (neglecting rounding errors for the moment) if all minors of the matrix in (46) are non-singular.

The algorithm consists of two steps. Forward elimination

$$\begin{aligned} H_1 &= -B_1^{-1}C_1 \\ H_n &= -[B_n + A_n H_{n-1}]^{-1}C_n, & n = 2, \dots, N-1 \\ g_1 &= B_1^{-1}k_1 \\ g_n &= [B_n + A_n H_{n-1}]^{-1}(k_n - A_n g_{n-1}), & n = 2, \dots, N \end{aligned} \quad (51)$$

Backward substitution

$$\begin{aligned} x_N &= g_N \\ x_n &= g_n + H_n x_{n+1}, & n = N-1, \dots, 1 \end{aligned} \quad (52)$$

In these notations the explicit form of the matrix coefficients

$$A_k^n = \begin{bmatrix} a_1 & a_3 \\ a_2 & a_4 \end{bmatrix}_{j-1}^n; \quad B_k^n = \begin{bmatrix} b_1 & b_3 \\ b_2 & b_4 \end{bmatrix}_j^n; \quad C_k^n = \begin{bmatrix} c_1 & c_3 \\ c_2 & c_4 \end{bmatrix}_{j+1}^n,$$

where matrix coefficients are given by equations (47) - (50).

To find the solution for the new velocities the following variables in the equations (47) - (50) have to be calculated

- face centered values of the thermodynamic variables;
- coefficients of the virtual mass;
- friction terms;
- velocities at the input/output valves.

The corresponding calculations are discussed in the following sections.

5.2.5 The face-centered values

The face-centered thermodynamic variables are interpolated between neighboring cell values based on the length of each half cell

$$\psi_j = \frac{\psi_{L-1} l_{L-1} + \psi_L l_L}{l_{L-1} + l_L}, \quad (53)$$

where ψ represents densities and void fractions for liquid and gas.

5.2.6 The coefficient of the virtual mass

Following [RELAP5-I] we introduce the coefficient of the virtual mass in the form

$$M_V = \begin{cases} \frac{1}{2} \frac{(1+2\alpha)}{1-\alpha} & \text{for } 0 \leq \alpha < 1/2, \\ \frac{1}{2} \frac{3-2\alpha}{\alpha} & \text{for } 1/2 \leq \alpha \leq 1. \end{cases}$$

The common multiplier for this coefficient remains a fitting parameter established on the basis of numerical experiments.

5.2.7 Friction terms

One of the difficulties of the pressure based solvers on the staggered grid is the approximation of the momentum equation for abruptly changing pipe diameter. A quasi-steady approximation is used in [RELAP5-I] and continuity of the volumetric flow is used in [TRACE] to mitigate this problem.

In the current simplified version of the code the following approach is adopted. The friction coefficients f_g , f_l , and f_i in equations (37) and (38) are determined using Churchill [Churchill77] approximation for all flow regimes (54)

$$f_w = 2 \left[\left(\frac{8}{Re} \right)^{12} + \frac{1}{(a+b)^{3/2}} \right]^{1/12}, \quad (54)$$

with Reynolds numbers

$$Re_{m,L} = \frac{\rho_{m,L} u_{m,L} D_{m,L}}{\mu_{g(l)}}$$

based on volume centered velocities $u_{m,L}$ given by (45) and hydraulic diameter

$$D_m = \frac{4 A_L}{l_{m,L}}$$

for each control volume. Here m takes values $m = \{g, l, i\}$ for gas, liquid, and interface in a given control volume.

Next, the major losses are presented in the form (39). And the minor losses are given by

$$F_{ml} = \alpha_m A K_{ml} \frac{\rho_m u_m |u_m|}{2}.$$

Here we have assumed a simple version of partitioning minor losses between phases. According to this equation for the sum of the momenta with equal velocities the homogeneous mixture has the same losses as liquid single phase. A more elaborated versions of the minor losses partitioning in the two-phase flow will be considered later.

With the simplified partitioning the sum of the major and minor losses for a given control volume can be written in the form

$$(f_m l_m \Delta x + \alpha_m A K_{ml}) \frac{\rho_m u_m^2}{2} = (F_m \Delta x + K_{ml}) A \alpha_m \rho_m u_m \frac{|u_m|}{2}, \quad (55)$$

where

$$F_m = f_m \frac{l_m}{\alpha_m A} \frac{|u_m|}{2} \quad \text{and} \quad K_{ml} = f_m \frac{l_{ml}}{D}.$$

Here l_{ml} effective pipe length corresponding to minor losses.

In the proposed above simplified approach minor losses are added to the major losses. Partitioning of the minor losses in a more general case will be discussed elsewhere.

5.2.8 Boundary conditions for the velocity matrix

Boundary conditions for the velocity matrix are determined by the liquid/gas flow through the input/output valves. The flow through the valves is assumed incompressible as was discussed in Sec. 4.5 and the corresponding 2×2 boundary matrices A , B , and C in the velocity matrix are of the form

$$A = \begin{pmatrix} 0 & 0 \\ 0 & 0 \end{pmatrix}, \quad B = \begin{pmatrix} 1 + \frac{dt}{\tau} & 1 + \frac{dt}{\tau} \\ 1 + \frac{dt}{\tau} & -1 - \frac{dt}{\tau} \end{pmatrix}, \quad C = \begin{pmatrix} 0 & 0 \\ 0 & 0 \end{pmatrix},$$

while the vector k is written as follows

$$k = \begin{bmatrix} u_{g0}^{n+1} + u_{l0}^{n+1} - \frac{(u_g^n + u_l^n)dt}{\tau} \\ u_{g0}^{n+1} - u_{l0}^{n+1} - \frac{(u_g^n - u_l^n)dt}{\tau} \end{bmatrix}$$

where

$$u_{g(l)0}^{n+1} = \frac{K_v}{A_v} \sqrt{\Delta p^{n+1} \left(\frac{\rho_w}{\rho_g(l)} \right)}, \quad (56)$$

where A_v is the pipe diameter fitted to the valve, K_v is the flow coefficient, Δp is the pressure drop across the valve, and $\rho_g(l)$ is the density of the fluid flowing through the valve. It is assumed that the void fraction and the temperature of the fluid are the same as in the upwind control volume.

5.2.9 Structure of the solver for velocities

To complete this section we briefly outline the structure of the solver for the new velocities. The following values are calculated at this sub-step:

1. Face centered values of thermodynamic variables;
2. Source terms for friction and inter-phase mass fluxes
 - Gas wall friction;

- Liquid wall friction;
 - Interface friction and
 - Face centered interphase mass fluxes.
3. Coefficient of the virtual mass;
 4. Face centered mixture density;
 5. Face centered density difference;
 6. Volume centered velocities;
 7. Boundary conditions;
 8. Coefficients for matrices in block diagonal matrix A_i , B_i , and C_i ;
 9. Coefficients of the free vector;

Once these calculations are completed one can solve block tridiagonal matrix and update velocities. When new velocities and new pressures are found, the provisional values of the densities, energies, void fraction, and temperatures can be found as described below.

5.3 Provisional values of thermodynamic variables

To find provisional values of thermodynamic variables new velocities are substituted back into equation (30), which is then solved with respect to dp_L^{n+1} , $de_{g,L}^{n+1}$, $de_{l,L}^{n+1}$, and $d\alpha_{g,L}^{n+1}$. The solution for the pressure is obtained in the form

$$dp_L^{n+1} = a_p^L du_{g,j+1}^{n+1} + b_p^L du_{g,j}^{n+1} + c_p^L du_{l,j+1}^{n+1} + d_p^L du_{l,j}^{n+1} + e_p^L,$$

and for the void fraction in the form

$$d\alpha_{g,L}^{n+1} = a_a^L du_{g,j+1}^{n+1} + b_a^L du_{g,j}^{n+1} + c_a^L du_{l,j+1}^{n+1} + d_a^L du_{l,j}^{n+1} + e_a^L, \quad (57)$$

with $a_a = (A_x^n)_1^{-1} a_x^n$, $b_a = (A_x^n)_1^{-1} b_x^n$, $c_a = (A_x^n)_1^{-1} c_x^n$, $d_a = (A_x^n)_1^{-1} d_x^n$, $e_a = (A_x^n)_1^{-1} e_x^n$.

Similarly, we have for the change of the gas energy $de_{g,L}^{n+1}$

$$de_{g,L}^{n+1} = a_{e,g}^L du_{g,j+1}^{n+1} + b_{e,g}^L du_{g,j}^{n+1} + c_{e,g}^L du_{l,j+1}^{n+1} + d_{e,g}^L du_{l,j}^{n+1} + e_{e,g}^L, \quad (58)$$

with $a_{e,g} = (A_x^n)_2^{-1} a_x^n$, $b_{e,g} = (A_x^n)_2^{-1} b_x^n$, $c_{e,g} = (A_x^n)_2^{-1} c_x^n$, $d_{e,g} = (A_x^n)_2^{-1} d_x^n$, $e_{e,g} = (A_x^n)_2^{-1} e_x^n$,

and for the change of the liquid energy $de_{l,L}^{n+1}$

$$de_{l,L}^{n+1} = a_{e,l}^L du_{g,j+1}^{n+1} + b_{e,l}^L du_{g,j}^{n+1} + c_{e,l}^L du_{l,j+1}^{n+1} + d_{e,l}^L du_{l,j}^{n+1} + e_{e,l}^L, \quad (59)$$

with $a_{e,l} = (A_x^n)_3^{-1} a_x^n$, $b_{e,l} = (A_x^n)_3^{-1} b_x^n$, $c_{e,l} = (A_x^n)_3^{-1} c_x^n$, $d_{e,l} = (A_x^n)_3^{-1} d_x^n$, $e_{e,l} = (A_x^n)_3^{-1} e_x^n$.

Once values of the energy and pressure are found one can calculate provisional values of densities and temperatures. For the densities we use the following expressions

$$\tilde{\rho}_{g,L}^{n+1} \approx \rho_{g,L}^n + \left(\frac{\partial \rho}{\partial p}\right)_{g,L}^n dp_L^{n+1} + \left(\frac{\partial \rho}{\partial e}\right)_{g,L}^n de_{g,L}^{n+1}; \quad (60)$$

$$\tilde{\rho}_{l,L}^{n+1} \approx \rho_{l,L}^n + \left(\frac{\partial \rho}{\partial p}\right)_{l,L}^n dp_L^{n+1} + \left(\frac{\partial \rho}{\partial e}\right)_{l,L}^n de_{l,L}^{n+1}. \quad (61)$$

similarly for the temperatures we obtain

$$\tilde{T}_{g,L}^{n+1} \approx T_{g,L}^n + \left(\frac{\partial T}{\partial p}\right)_{g,L}^n dp_L^{n+1} + \left(\frac{\partial T}{\partial e}\right)_{g,L}^n de_{g,L}^{n+1}; \quad (62)$$

$$\tilde{T}_{l,L}^{n+1} \approx T_{l,L}^n + \left(\frac{\partial T}{\partial p}\right)_{l,L}^n dp_L^{n+1} + \left(\frac{\partial T}{\partial e}\right)_{l,L}^n de_{l,L}^{n+1}. \quad (63)$$

Using provisional values of the densities and temperatures one can update the values of the heat and mass fluxes following the results of Sections 4.3 and 4.4. The updated intermediate values of the mass and heat fluxes can be used in the second step of the code. The details of the calculations at the 2nd step are provided below.

6 Second step

At the second step of the algorithm the unexpanded form of the gas density

$$\begin{aligned} d(\alpha\rho)_{g,L}^{n+1} + \left(d(\alpha\rho)_{g,j+1}^{n+1} + (\alpha\rho)_{g,j+1}^n\right) u_{g,j+1}^{n+1} \frac{A_{j+1}\Delta t}{V_L} - \\ \left(d(\alpha\rho)_{g,j}^{n+1} + (\alpha\rho)_{g,j}^n\right) u_{g,j}^{n+1} \frac{A_j\Delta t}{V_L} = \frac{\tilde{\Gamma}_{g,L}^n \Delta t}{V_L}, \end{aligned} \quad (64)$$

liquid density

$$\begin{aligned} d(\alpha\rho)_{l,L}^{n+1} + \left(d(\alpha\rho)_{l,j+1}^{n+1} + (\alpha\rho)_{l,j+1}^n\right) u_{l,j+1}^{n+1} \frac{A_{j+1}\Delta t}{V_L} \\ - \left(d(\alpha\rho)_{l,j}^{n+1} + (\alpha\rho)_{l,j}^n\right) u_{l,j}^{n+1} \frac{A_j\Delta t}{V_L} = -\frac{\tilde{\Gamma}_{g,L}^n \Delta t}{V_L}, \end{aligned} \quad (65)$$

gas energy

$$\begin{aligned} (\alpha\rho e)_{g,L}^{n+1} + \left(d(\alpha\rho e)_{g,j+1}^{n+1} + (\alpha\rho e)_{g,j+1}^n + (\alpha\rho)_{g,j+1}^n p_L^{n+1}\right) u_{g,j+1}^{n+1} \frac{A_{j+1}\Delta t}{V_L} - \\ \left(d(\alpha\rho e)_{g,j}^{n+1} + (\alpha\rho e)_{g,j}^n + (\alpha\rho)_{g,j}^n p_L^{n+1}\right) u_{g,j}^{n+1} \frac{A_j\Delta t}{V_L} = \\ -p_L^n d\tilde{\alpha}_{g,L}^n + \left(\tilde{H}_{wg,L}^n \left(\tilde{T}_{w,L}^n - \tilde{T}_{g,L}^n\right) S_{wg,L}^n + \tilde{\Gamma}_{g,L}^n \tilde{H}_{g,L}^n\right) \frac{\Delta t}{V_L}, \end{aligned} \quad (66)$$

and liquid energy

$$\begin{aligned} d(\alpha\rho e)_{l,L}^{n+1} + \left(d(\alpha\rho e)_{l,j+1}^{n+1} + (\alpha\rho e)_{l,j+1}^n + (\alpha\rho)_{l,j+1}^n p_L^{n+1}\right) u_{l,j+1}^{n+1} \frac{A_{j+1}\Delta t}{V_L} - \\ \left(d(\alpha\rho e)_{l,j}^{n+1} + (\alpha\rho e)_{l,j}^n + (\alpha\rho)_{l,j}^n p_L^{n+1}\right) u_{l,j}^{n+1} \frac{A_j\Delta t}{V_L} = \\ p_L^n d\tilde{\alpha}_{g,L}^n + \left(\tilde{H}_{wl,L}^n \left(\tilde{T}_{w,L}^n - \tilde{T}_{l,L}^n\right) S_{wl,L}^n - \tilde{\Gamma}_{g,L}^n \tilde{H}_{l,L}^n\right) \frac{\Delta t}{V_L}. \end{aligned} \quad (67)$$

equations are solved implicitly using values for the new velocities and pressures, and provisional values for the temperature, heat transfer coefficients, and mass fluxes obtained at the previous step.

6.1 Tri-diagonal form of the matrix equations

The efficient solution of the equations (64) - (67) can be obtained by noticing that all four equations are independent and have the same structure

$$dU_L^{n+1} + dU_{j+1}^{n+1}\gamma_{j+1}^{n+1} - dU_j^{n+1}\gamma_j^{n+1} = S_L, \quad (68)$$

where $\gamma_{j+1}^{n+1} = u_{j+1}^{n+1} \frac{A_{j+1}\Delta t}{V_L}$ and the upwind values of the conservative variables dU_{j+1}^{n+1} can be represented in the form

$$dU_j^{n+1} = \lambda_j^{n+1} dU_{L-1}^{n+1} + \mu_j^{n+1} dU_L^{n+1}. \quad (69)$$

The eq. (69) for the density and for the energy has the form of equation (32) and equation (33) correspondingly.

By substituting (69) into (68) all four equations (64) - (67) can be re-written in the standard tridiagonal form

$$a_L dU_{L-1}^{n+1} + b_L dU_L^{n+1} + c_L dU_{L+1}^{n+1} = S_L, \quad (70)$$

where $a_L = -\lambda_j^{n+1}\gamma_j^{n+1}$, $b_L = 1 + \lambda_{j+1}^{n+1}\gamma_{j+1}^{n+1} - \mu_j^{n+1}\gamma_j^{n+1}$, and $c_L = \mu_{j+1}^{n+1}\gamma_{j+1}^{n+1}$ are coefficients of the sub-diagonal, main diagonal, and super-diagonal of the tridiagonal matrix.

The structure of the S_L terms is clear from the equations (64) - (67). Here we provide as an example the structure of the S_L term for the first equation (64)

$$S_{g,L} = \frac{\tilde{\Gamma}_{g,L}^n \Delta t}{V_L} - (\alpha\rho)_{g,j+1}^n \gamma_{g,j+1}^{n+1} + (\alpha\rho)_{g,j}^n \gamma_{g,j}^{n+1}. \quad (71)$$

The tridiagonal equation (70) can be efficiently solved using standard tridiagonal solvers (see e.g. [Thomas49, LuchDG-I]). Note that coefficients a_L , b_L , and c_L for the tridiagonal matrix are the same for the density and energy equations. These coefficients are calculated only once for each pair of the conservation equations.

Once conservative variables are calculated the density and energy for the gas and for the liquid can be found as follows.

6.2 Calculation of the main dynamical variables

Obtained conservative variables for the density and energy

$$\left\{ (\alpha\rho)_{g,L}^{n+1}, (\alpha\rho)_{l,L}^{n+1}, (\alpha\rho e)_{g,L}^{n+1}, (\alpha\rho e)_{l,L}^{n+1} \right\}$$

are used to find primitive variables

$$e_{g,L}^{n+1} = (\alpha\rho e)_{g,L}^{n+1} / (\alpha\rho)_{g,L}^{n+1}; \quad e_{l,L}^{n+1} = (\alpha\rho e)_{l,L}^{n+1} / (\alpha\rho)_{l,L}^{n+1}.$$

and

$$\alpha_{l,L}^{n+1} = (\alpha\rho)_{l,L}^{n+1} / \tilde{\rho}_{l,L}^{n+1}; \quad \alpha_{g,L}^{n+1} = 1 - \alpha_{l,L}^{n+1}; \quad \rho_{g,L}^{n+1} = (\alpha\rho)_{g,L}^{n+1} / \alpha_{g,L}^{n+1}.$$

Note that in the first equation above the provisional value of the liquid density is used to obtain liquid void fraction.

It is important to emphasize that it is the efficiency of the three main solvers (for the set of expanded equations (26) - (29), for the velocity matrix (46), and for the set of unexpanded equations (64) - (67)) that render the nearly implicit algorithm as one of the most efficient methods for solution of the two-phase flow problem.

For the one dimensional two-phase flow problems the number of iterations scales linearly in time for this algorithm. For cryogenic loading system with up to 100 control volumes the integration time is a few hundreds times faster than the real time. Short integration time paves the way to the on-line optimization of the mitigation strategies making nearly implicit algorithm very attractive for applications to the on-line control of loading operations.

However, stability of the algorithm poses a long standing problem of the two-phase flow research (see e.g. [Nourgaliev, LuchDG-I]) and requires a special attention. Stabilization techniques that are employed in the current version of the code are discussed briefly in the following section.

7 Control

The control module consists of three main blocks. In the first block the dynamical variables are reset to the limiting values when these values are outside of the predefined range. In the second block the values of the dynamical variables are smoothed during phase appearance/disappearance. And in the third block the time step is reset when the deviation from the mass conservation is detected and when the values of the thermodynamic variables are changed abruptly or lie outside the physical range.

In addition, the opening of the dump valves is controlled to limit the mass losses during one time step by values less or equal to 10% of the remaining mass.

7.1 Direct control of the dynamical variables

At the first control step the values of the thermodynamic variables are checked against their saturation values. If the phasic density or energy is beyond corresponding limiting saturation value it is reset to the saturation value. This simplification is adopted because in the present version

of the code the subcooled gas state and superheated liquid state are not allowed. In the future versions of the code the correlations module will be extended by including superheated liquid and sub-cooled gas states.

At the first control step we also check void fractions against the minimum and maximum values. If the void fractions are beyond the limiting values (that are usually set at 1×10^{-7} and $1 - 1 \times 10^{-7}$) they are reset to the corresponding limiting values.

7.2 Smoothing of the dynamical variables during phase appearance/disappearance

At the second step of the control module the void fractions are checked against the smoothing margins. In this work, we follow recommendations by Liou [Liou07] and adjust temperature, velocity, and density according to the following expression

$$\phi_{adj} = g(x)\phi_d + (1 - g(x))\phi_c, \quad (72)$$

where

$$g(x) = x^2(2x - 3); \quad \text{and} \quad x = \frac{\alpha_d - x_{\min}}{x_{\max} - x_{\min}}.$$

Here “d” stands for disappearing phase and “c” for conducting phase. The role of the limiters and smoothers described in this section is critical for the code stabilization. The exact values of the minimum and maximum void fraction, for which smoothing (72) is applied should be established using extensive numerical experimentation. Currently these values are set at the 1×10^{-7} and 1×10^{-2} .

7.3 Time step control

At the third step of the control module a time step of the algorithm is reset. Multiple checks are performed that can through a flag to reduce the time step of the integration. Firstly, it is insured that the changes of the densities, energies, and pressures during one integration step do not exceed 25% of their absolute values at the previous time step. Secondly, we test if the results of the calculations for the pressure and temperature are outside of the predefined range of values. Thirdly, we check if the predictions of the density and the temperature obtained using the Taylor expansion during the 1st step of integration do not deviate too much from the corresponding corrected values obtained by solving unexpanded set of conservation equations during the 2nd step. Finally, we control the deviation from the mass conservation by monitoring the overall changes of the mass in the transfer line and the total mass flow in and out of the transfer line through the valves.

For example, let us discuss in more details the control of the deviation of the corrected densities from the predicted values. The total density

for each control volume

$$\rho_{m,L}^{n+1} = \alpha_{g,L}^{n+1} \rho_{g,L}^{n+1} + (1 - \alpha_{g,L}^{n+1}) \rho_{l,L}^{n+1}$$

is calculated using solution of the unexpanded form of the mass and energy conservation equations at the second step of the algorithm as shown in Sec. 6. These total densities are compared to the densities obtained by Taylor expansion

$$\begin{aligned} \tilde{\rho}_{m,L}^{n+1} = & \tilde{\alpha}_{g,L}^n \left(\rho_{g,L}^n + \left(\frac{\partial \rho}{\partial p} \right)_{g,L}^n dp_L^{n+1} + \left(\frac{\partial \rho}{\partial e} \right)_{g,L}^n de_{g,L}^{n+1} \right) + \\ & \tilde{\alpha}_{l,L}^n \left(\tilde{\rho}_{l,L}^n + \left(\frac{\partial \rho}{\partial p} \right)_{l,L}^n dp_L^{n+1} + \left(\frac{\partial \rho}{\partial e} \right)_{l,L}^n de_{l,L}^{n+1} \right) \end{aligned}$$

The maximum error for each control volume and the total error are found as follows

$$Err_{\max} = \max \left(\frac{\rho_{m,L}^{n+1} - \tilde{\rho}_{m,L}^{n+1}}{\tilde{\rho}_{m,L}^{n+1}} \right), \quad Err_{tot} = \frac{2 \sum_L \left(\rho_{m,L}^{n+1} - \tilde{\rho}_{m,L}^{n+1} \right)^2}{\sum_L \left(\tilde{\rho}_{m,L}^{n+1} \right)^2}.$$

If either of these errors is larger than 10^{-2} the time step is halved and the integration step is repeated.

7.4 Dump valve control

Since the flow through the transfer line is actively controlled by the dump valves we have to ensure that there is no liquid flow through the dump valves in nominal loading regime. This is done in two ways. First, if the gas void fraction in a given control volume is between 0.2 and 0.05 the flow through the dump valve is smoothly reduced to 0 using smoother (72). Next, we check if the mass loss through the dump valve during one time step is smaller than 10% of the mass of the gas in the associated control volume. If it is not the time step is halved and the integration step is repeated.

7.5 Code termination

During integration the values of the key thermodynamic variables may occasionally be found to lie outside predefined range as described above. If this happens the time step is halved. The reduction of the time step continues until reached the minimum predefined value (usually 10 mks). If all the field values are found to be inside the range, and both mass errors are smaller than 10^{-2} , the time step is reset to the maximum predefined value. The time step of integration is usually between 10 ms and 20 ms.

If the integration time is smaller than a predefined limiting value and one of the errors discussed above still prevails the integration is terminated.

Extensive numerical testing shows that the control of the thermodynamic values and of the integration time step outlined above guarantees a stable and robust performance of the algorithm during cryogenic loading in a wide range of the system parameters with time step up to 20 ms. Despite the simplified set of correlations the results of integration are in reasonable agreement with the experiment data. The comparison with the experimental data will be discussed in more details in the next section.

8 Comparison with the experimental data

In this section we briefly describe some of the key features of the algorithm and discuss a comparison of the model predictions with the experimental data of chilldown in the cryogenic transfer line.

8.1 Some key features of the algorithm

Partial verification and validation of the nearly implicit algorithm was discussed in our earlier report [LuchDG-II]. The original simplified version was written in MATLAB. Its main goal was to prove the capability of the method to deal with cryogenic loading and chilldown problems. The integration was performed on a uniform grid and the integration time was of the order of 80% of real time.

Using this simplified version we demonstrated the capability to simulate pressure waves and material waves, in particular, gravitational waves in the pipes. We demonstrated the phase separation due to gravity force, emptying the pipe filled initially with liquid, and vapor locking phenomenon in the regime when initially empty pipe is filled by the evaporating liquid. We also demonstrated the code capability to simulate valves closing and opening and mitigation of the vapor lock fault during chilldown by opening dump valve. Finally, we performed initial validation of the model by comparing the results of simulations with the experimental data obtained during first 300 sec of chilldown of the cryogenic testbed.

The C++ version of the algorithm discussed in the present report preserves the properties of the original code listed above and offers a number of improvements. We have added the ability to integrate two-phase flow equations on an arbitrary non-uniform grid. The code was restructured and optimized to allow for much faster integration. The upgraded version currently runs up to 400 times faster than the real time. Such an acceleration paves the way to the on-line optimization of the mitigation strategies, which is important for efficient autonomous control.

Another feature of the accelerated code is its ability to perform efficiently search in the multi-dimensional parameter space of the correlation functions. This is essential for autonomous control of loading,

because the corresponding correlations are not well-known for cryogenic fluids and continuous on-line learning of the correlations is required to improve accuracy and reliability of the fault detection, identification and recovery.

The analysis of the full set of correlations and their effect on the accuracy of the model predictions will be given in a separate report [LuchDG-III]. A brief preview of required correlations that include flow patterns recognition and calculations of the frictional losses, heat and mass transfer was given in this report in Sections 4 and 5.2.7. Below we describe briefly a comparison of the predictions of the accelerated model with experimental results using a simplified set of correlations. Despite the adopted simplifications the agreement with the experimental data was substantially improved as compared to the results reported [LuchDG-II] and extended from 300 sec to the 1600 sec of chilldown.

8.2 Loading regime

During chilldown at the KSC testbed the pipes and the vehicle tank are initially filled with hot nitrogen gas at $T = 300K$ and $p = 1$ atm. The storage tank is filled with liquid nitrogen at $T = 80K$ and $p = 3.245$ atm. At time 0 the input valve MV151 is opened manually. It takes approximately 15 sec to open this valve, however, the exact opening dynamics is unknown. The main control valve Ro115 remains closed for another 195 sec preventing flow through transfer line. During this pre-chilldown time two dump valves (dvc112 and dvc117, see Fig. 13) are opened at approximately at 145 and 163 sec to chill the first section of the transfer line.

At approximately 195 sec the main control valve Ro115 is opened and the line is chilled and filled with liquid nitrogen during next 1400 sec. The flow variations depends mainly on the boiling dynamics and on the relative opening of the dump valves. The flow boiling dynamics is highly non-trivial process and will be considered in details in a separate report [LuchDG-III]. The valve opening, on the other hand is well defined and controlled remotely by the operators in the control room. Therefore an accurate simulation of the valve opening is a prerequisite for inferring the parameters of the flow boiling in the transfer line. The valve opening time-series are embedded into the code in the form of tables. The opening at arbitrary time is interpolated using these tables.

The comparison of the actual opening with the interpolated values is shown in the Fig. 13. It can be seen from the figure that the dump valves and the line valves are operating according to their actual nominal behavior. The effect of the dump valve opening and closing on the liquid flow was verified earlier (see Sec. 6.5 in [LuchDG-II]). We now describe the comparison between the time-series data and model predictions for the pressure and temperature.

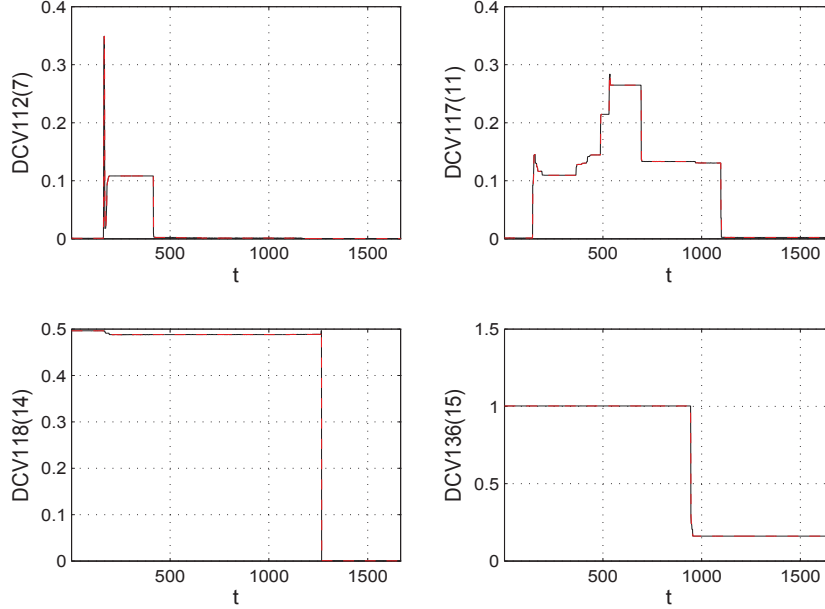


Figure 13. Relative valves opening for the valves cv112, cv117, cv118, cv136. The experimental time-series (black line) as compared to the interpolated values (red dashed lines).

8.3 Pressure

During the simulations that are discussed below the following simplifications were introduced in the correlation module. No heat exchange was allowed between the phases. The heat exchange was between the gas and the wall, the liquid and the wall, and the environment and the wall was included. The rates of vaporization and the heat exchange are taken as constants. The flow is modeled as conceptually stratified (i.e. the flow regime is assumed to be stratified flow for all parameters).

The simulations of the first 1600 sec of the chilldown process is shown in the Fig. 14 in comparison with the experimental pressure time-series data. It can be seen from the figure that the model can reproduce quite accurately the pressure drop along the pipe and the pressure oscillations during opening of the input valve MV151 and the main transfer valve Ro115. It can also reproduce the pressure jump at 195 sec at the location of the sensor PT161 and the distribution of the pressure along the system (cf the change of the absolute pressure along the transfer line at the locations PT PT102, PT157, PT161, PT148 in the figure).

The simplified character of the correlations can be inferred by noticing the overestimation of the pressure level at the location PT161 by 16% for $t \geq 500$ sec and significant overestimation of the pressure oscillation at location PT148 at around 500 sec. These deviations are attributed to

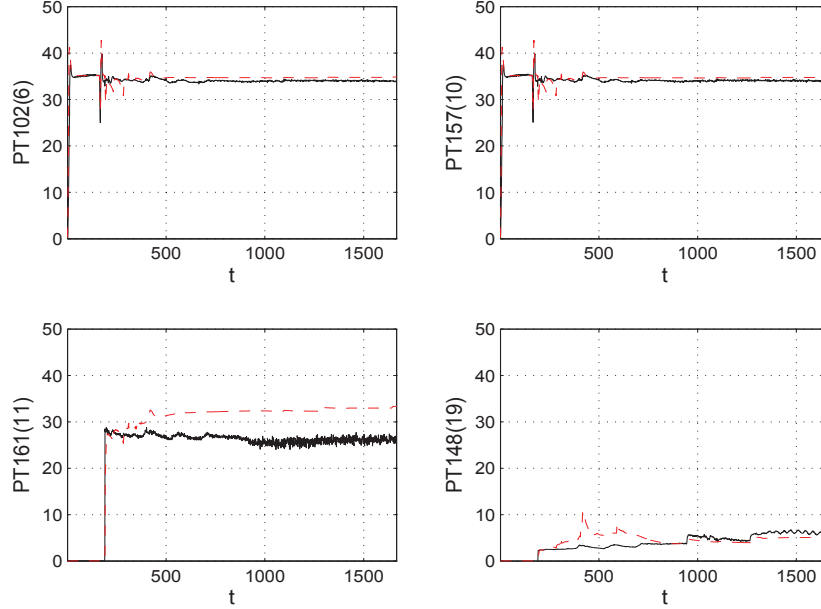


Figure 14. Experimental time-series of pressure (black lines) in comparison with model predictions (red dashed lines) for 6 sensors: PT102, PT157, PT161, PT148.

the two main factors.

Firstly, the only two-phase flow regime recognized in the simplified version is stratified flow. As a result, the liquid propagates quickly to the end of the transfer line while being in the contact with the hot wall. This leads to overestimation of the evaporation rates in the control volumes closer to the end of the line. Secondly, the heat transfer rate in the simplified version is taken to be a constant approximately equal to the average heat transfer rate in the film boiling regime. This leads to an additional overestimation of the heat transfer rate. The overestimation is especially strong closer to the end of the transfer line where dryout, dispersed, and mist flow regimes are expected to dominate during chilldown. The overestimation of the heat transfer leads to the overestimation of the mass flow and as a result to an increased pressure level in the end of the line. This simplifications will be lifted in the next version of the algorithm as will be described in the next report [LuchDG-III].

8.4 Temperature

The model predictions for the temperature are compared with the experimental time-series data in the Fig. 15. A good agreement between the simulated and measured data can be seen un the figure. In particular, a good agreement observed at the location of sensor TT202 during first

200 sec is a substantial improvement as compared to the earlier results (see Sec. of [LuchDG-II]).

This improvement was achieved by taking into account an additional section of the pipe that is located before valve MV151 and exposed to direct radiation. The corresponding changes included into the model geometry allowed for a better agreement with the experimental data not only at the location of sensor TT202, but also at all other locations as can be seen in the figure.

However, the simplified character of the correlations used at this stage of the research do not allow to model a number of important features of the chilldown process. For example, strong oscillations of the temperature observed during cryogenic loading at KSC testbed could not be accurately reproduced in simulations.

There are two main problems already mentioned at the end of the previous section. The first one is related to the fact that the current version recognizes only three flow regimes: (i) pure liquid; (ii) pure gas; and (iii) stratified flow. Second problem is that heat transfer coefficients are considered to be constants in the whole temperature range of the gas and liquid flow.

As a result the strong peak in the heat transfer corresponding to the nucleate and transition boiling regimes (see Fig. 9) is not taken into

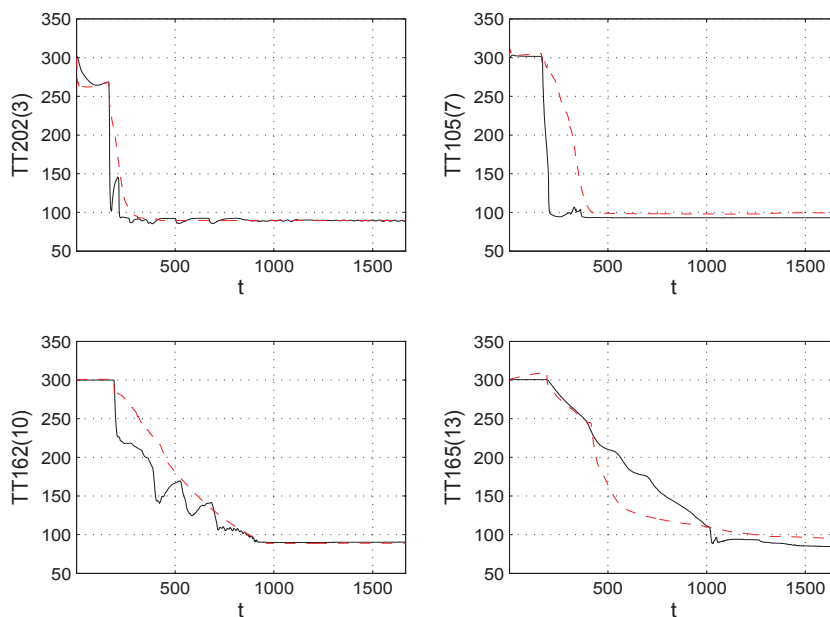


Figure 15. Experimental time-series of temperature (black lines) in comparison with model predictions (red dashed lines) for 6 sensors: TT202, TT105, TT162, TT165.

account. But it is this peak in heat (and accordingly in the mass) transfer rates that is responsible for the fast temperature drop observed in the experiment at approximately 167 sec in the top two figures and at 190 and 395 sec in the bottom left figure of the Fig. 15. Such a fast cooling due to extensive evaporation can also cause a significant vapor lock with subsequent temperature raise as can be seen in the figure. To reproduce these features in the simulations a more accurate correlations that take into account the details of the boiling cure are required.

Another deviation of the model predictions from the experimental data can be observed at the location of the sensor TT165. It can be seen from the figure that the model predicts faster temperature drop than observed during the test at around 500 sec. This result indicates the fact that the simplified version of the correlation module can only recognized stratified flow. As a result the heat transfer rate is overestimated in dispersed flow regimes observed experimentally at this location causing a faster temperature drop as compared to the experimental results (see temperature time-traces between 420 and 1000 sec in the bottom right figure of the Fig. 9). To avoid this problem the dispersed flow regime will be included in the next version of the code.

Further details of the correlation module and the effect of the correlation parameters on the accuracy of the model predictions will be given in a separate report [LuchDG-III].

9 Conclusions

In this report we discussed the details of the nearly-implicit method as it was coded in the C++ version of the algorithm. We described calculations performed in the following main modules of the algorithm: (i) geometry; (ii) boundary conditions; (ii) correlations; (iii) first step, including solution of the expanded equations and of the velocity matrix; (iv) second step; and (v) control module.

The following new features were added to the code as compared to the version discussed in the first two reports [LuchDG-I, LuchDG-II]: (i) the ability to integrate two-phase flow on an arbitrary non-uniform 1D grid; (ii) improved module structure of the code that allows for more efficient computation and extends flexibility if the code with respect to future modifications; (iii) reduced integration time was achieved due to translation to C++, extensive use of tables and linear interpolations, explicit coding of the matrix inverse for expanded conservation equation and improved efficiency of the memory management; currently the integration is up to 400 times faster than real time; (iv) updated the correlation module. As a result the code is faster, more stable and allows for more accurate model predictions of the pressure and temperature dynamics.

Substantial acceleration and improved accuracy of the C++ version

of the algorithm paves the way for the future development of the on-line fault detection, isolation and recovery methods of loading control. These features make this method attractive for applications to autonomous control of cryogenic loading.

However, the comparison of the results of simulations with the experimental data also reveals some limitations of the current version. In particular, it was shown that temperature oscillations and vapor lock could not be accurately reproduced at some locations during initial stage of chilldown. Our analysis has shown that these limitations can be alleviated by extending the correlation module. It was suggested that the next version of the correlation module should recognize more flow regimes of the two-phase flow and model more accurately the boiling curve under various flow conditions. The results of these improvements will be discussed in a separate technical report [LuchDG-III].

Nomenclature

Acronyms

Δx	length of control volume
\dot{q}	heat flux
A	pipe cross-section area
b_l	height of the liquid level in the pipe
D	pipe diameter
E	total specific energy
e	internal specific energy
F	friction factor
f	friction coefficient
H	specific enthalpy
h	heat transfer coefficient
h_c, h_{fc}	convection and forced convection heat transfer coefficients
H_{lg}	latent heat transfer of evaporation
l	perimeter of control volume
M_V	coefficient of the virtual mass
p	pressure
Pr	Prandtl number

Re	Reynolds number
S	wall area of control volume
T	temperature
u	velocity
z	height of control volume center above the ground

Greek Symbols

α	gas void fraction
β	liquid void fraction
χ_{tt}	Lockhart-Martinelli parameter
Γ	mass flux
κ	thermal conductivity
μ	viscosity
ρ	density
σ	surface tension
τ	drag force

Superscripts

$\bar{\psi}$	upwind value
$\tilde{\psi}$	face centered value
n	index for the time step

Subscripts

$,t$	time partial derivative
$,x$	spatial partial derivative
dv	dump valve
g	gas
j	index for the staggered grid
L	index for the main grid
l	liquid
s	saturation value

References

- LuchDG-I. Luchinsky, D.G., Smelyansky, V.N., Brown, B., “Physics Based Model for Cryogenic Chillover and Loading. Part I: Algorithm”, NASA/TP 2013-N, Nov. 2013.
- LuchDG-III. Luchinsky, D.G., Smelyansky, V.N., Brown, B., “Physics Based Model for Cryogenic Chillover and Loading. Part III: Correlations”, NASA/TP 2014 (to be published).
- Liles-78. Liles, D.R. and Reed, Wm.H., “A Semi-Implicit method for two-phase fluid dynamics”, *Journal of Computational Physics*, 26:390407, 1978.
- Harlow-68. Harlow F. H., and Amsden, A. A., “Numerical calculation of almost incompressible flow”, *Journal of Computational Physics*, 3:8093, 1968.
- RELAP5-I. INEL, 2012. RELAP5/MOD3 Code Manual. Volume I: Code Structure, System Models and Solution Methods INEEL-EXT-98-00834-V1/Rev4, Vol. 1
- Nourgaliev. NOURGALIEV, R., CHRISTON, M., Solution Algorithms for Multi-Fluid-Flow Averaged Equations, INL/EXT-12-27187 (151 p.), September 27, 2012
- Cordier13. Cordier, F., Degond, P., Kumbaro, A., “Phase Appearance or Disappearance in Two-Phase Flows”, *Journal of Scientific Computing*, p. 1-34, 2013.
- Ransom89. Ransom, V. H., “Numerical Modeling of Two-Phase Flows for Presentation at Ecole d’Ete d’Analyse Numerique”, EGG-EAST-8546, 1989.
- TRACE. TRACE code development team. TRACE v5.0 Theory Manual: Field equations, Solution methods, and Physical models, 2007.
- Kattan:98a. Kattan, N, Thome, J. R., Favrat, D., “Flow Boiling in Horizontal Tubes: Part 2–New Heat Transfer Data for Five Refrigerants”, *Journal of Heat Transfer*, v. 120(1), p. 148-155, 1998.
- RELAP5-IV. INEL, 2012. RELAP5/MOD3 Code Manual. Volume IV: Models and Correlations, INEEL-EXT-98-00834, Volume IV, Revision 4.0.
- RELAP5-VI. Shieh, A.S., Ransom, H.V., Krishnamurthy, R., INEL, 2001. RELAP5/MOD3 Code Manual. Volume VI: Validation of numerical techniques in relap5/mod3.0, NUREG/CR-5535/Rev 1-Vol VI

- Churchill77. Churchill, S. W., "Friction Factor Equations Spans All Fluid-Flow Regimes", *Chemical Eng.*, November, 91-92, 1977.
- Taitel76. Taitel, Y. and Dukler, A.E. "A Model for Predicting Flow Regime Transitions in Horizontal And Near Horizontal Gas-Liquid Flow," *AIChE Journal*, 22 (1), 47-55, 1976.
- Staedtke. Staedtke, H., *Gasdynamic Aspects of Two-Phase Flow: Hyperbolicity, Wave Propagation Phenomena, and Related Numerical Methods*, Darmstadt: John Wiley & Sons, 2006.
- Yuan06. Yuan, K, *Cryogenic Boiling and Two-phase Chillover Process Under Terrestrial and Microgravity Conditions*: University of Florida; 2006.
- Kandlikar01. Kandlikar, S. G., "A Theoretical Model to Predict Pool Boiling CHF Incorporating Effects of Contact Angle and Orientation", *Journal of Heat Transfer* 123(6):1071-1079, 2001.
- Kutateladze48. Kutateladze, S. S., "On the transition to film boiling under natural convection", *Kotloturbostroenie* 3, 10, 1948.
- Zuber58. Zuber, N., "On stability of boiling heat transfer", *Transaction of ASME* 80, 711-720, 1958.
- Thomas49. Thomas, L.H., *Elliptic Problems in Linear Differential Equations over a Network*, Watson Sci. Comput. Lab Report, Columbia University, New York, 1949.
- Liou07. Chang, C. H., and Liou, M. S., "A robust and accurate approach to computing compressible multiphase flow: Stratified flow model and AUSM+-up scheme", *Journal of Computational Physics*, **225**, 840873, 2007.
- LuchDG-II. Luchinsky, D.G., Smelyansky, V.N., Sass, J., Brown, B., "Physics Based Model for Cryogenic Chillover and Loading. Part II: verification and validation", NASA/TP-2014-218298
- Wallis69. Wallis, G. B. *One-dimensional Two-phase Flow*, McGraw-Hill, New York, 1969.
- Reimar66. Reimar, F., *On stable methods of matrix factorization for block-tri-diagonal matrices, Part 1: General methods and theorems*, AEC research and development report, GA-7164, 1966
- NIST90. Lemmon, E. W., Huber, M. L., McLinden, M. O., *NIST Standard Reference Database 23: Reference Fluid Thermodynamic and Transport Properties - REFPROP*, 9.0, 2010

- Bridgman61. Bridgman, P. W., Thermodynamics of Electrical Phenomena in Metals and a Condensed Collection of Thermodynamic Formulas, New York: Dover, 1961.
- Bejan03. Bejan, A., Kraus, A. D., Heat Transfer Handbook: J. Willey, 2003
- Lockhart49. Lockhart, R. W. and Martinelli, R. C., "Proposed Correlation of Data for Isothermal Two-Phase, Two-Component Flow in Pipes," Chemical Engineering Progress, v. 45, pp. 39-48, 1949.
- Nellis09. Nellis, G, Klein, S., Heat Transfer: Cambridge University Press, 2009.
- Holman89. Holman, J.P., Heat transfer: McGraw-Hill, 1989.
- Bromley50. Bromley, L. A., Heat Transfer in Stable Film Boiling, Chemical Engineering Progress, 46, pp. 221-227, 1950.
- Sellers56. Sellers, J. R., Tribus, M., and Klein, J. S., Heat Transfer to Laminar Flows in a Round Tube or Flat Conduit: The Graetz Problem Extended, Transactions of the ASME, 78, p. 441, 1956.
- Dittus30. Dittus, F. W., and Boelter, L. M. K., Heat Transfer in Automobile Radiators of the Tubular Type, Publications in Engineering, 2, University of California, Berkeley, pp. 443-461, 1930.
- Churchill75. Churchill, S. W., and Chu, H. H. S., Correlating Equations for Laminar and Turbulent Free Convection From a Vertical Plate, International Journal of Heat and Mass Transfer, 18, pp. 1323-1329, 1975.
- Collier94. Collier JG, Thome JR. Convective Boiling and Condensation: Clarendon Press; 1994.
- Cooper84. Cooper, M. G., Saturation Nucleate Pool Boiling: A Simple Correlation, Department of Engineering Science, Oxford University, Oxford, pp. 86, 785793, 1984.

Note that this entry is not necessarily in the correct NASA format. Consult Technical Editing for correct reference format.

REPORT DOCUMENTATION PAGE				Form Approved OMB No. 0704-0188	
<p>The public reporting burden for this collection of information is estimated to average 1 hour per response, including the time for reviewing instructions, searching existing data sources, gathering and maintaining the data needed, and completing and reviewing the collection of information. Send comments regarding this burden estimate or any other aspect of this collection of information, including suggestions for reducing this burden, to Department of Defense, Washington Headquarters Services, Directorate for Information Operations and Reports (0704-0188), 1215 Jefferson Davis Highway, Suite 1204, Arlington, VA 22202-4302. Respondents should be aware that notwithstanding any other provision of law, no person shall be subject to any penalty for failing to comply with a collection of information if it does not display a currently valid OMB control number.</p> <p>PLEASE DO NOT RETURN YOUR FORM TO THE ABOVE ADDRESS.</p>					
1. REPORT DATE (DD-MM-YYYY) 01-11-2014		2. REPORT TYPE Technical Publication		3. DATES COVERED (From - To)	
4. TITLE AND SUBTITLE Physics Based Model for Cryogenic Chilldown and Loading. Part IV: Code Structure				5a. CONTRACT NUMBER	
				5b. GRANT NUMBER	
				5c. PROGRAM ELEMENT NUMBER	
6. AUTHOR(S) D. G. Luchinsky and V. N. Smelyanskiy and B. Brown				5d. PROJECT NUMBER	
				5e. TASK NUMBER	
				5f. WORK UNIT NUMBER	
7. PERFORMING ORGANIZATION NAME(S) AND ADDRESS(ES) NASA Ames Research Center Moffett Field, California 94035-2199				8. PERFORMING ORGANIZATION REPORT NUMBER L-12456	
9. SPONSORING/MONITORING AGENCY NAME(S) AND ADDRESS(ES) National Aeronautics and Space Administration Washington, DC 20546-0001				10. SPONSOR/MONITOR'S ACRONYM(S) NASA	
				11. SPONSOR/MONITOR'S REPORT NUMBER(S) NASA/TP-2014-218399	
12. DISTRIBUTION/AVAILABILITY STATEMENT Unclassified-Unlimited Subject Category 64 Availability: NASA CASI (443) 757-5802					
13. SUPPLEMENTARY NOTES An electronic version can be found at http://ntrs.nasa.gov .					
14. ABSTRACT This is the forth report in a series of technical reports that describe separated two-phase flow model application to the cryogenic loading operation. In this report we present the structure of the code. The code consists of five major modules: (i) geometry module; (ii) solver; (iii) material properties; (iv) correlations; and finally (v) stability control module. The two key modules - solver and correlations - are further divided into a number of submodules. Most of the physics and knowledge databases related to the properties of cryogenic two-phase flow are included into the cryogenic correlations module. The functional form of those correlations is not well established and is a subject of extensive research. Multiple parametric forms for various correlations are currently available. Some of them are included into correlations module as will be described in details in a separate technical report. Here we describe the overall structure of the code and focus on the details of the solver and stability control modules.					
15. SUBJECT TERMS CFD, grid					
16. SECURITY CLASSIFICATION OF:			17. LIMITATION OF ABSTRACT	18. NUMBER OF PAGES	19a. NAME OF RESPONSIBLE PERSON
a. REPORT	b. ABSTRACT	c. THIS PAGE			STI Help Desk (email: help@sti.nasa.gov)
U	U	U	UU	19	19b. TELEPHONE NUMBER (Include area code) (443) 757-5802
